Original Research

Green Synthesis and Adsorptive Performance of MOF-199/GO NCs for Efficient Removal of Organic Pollutants

Ahmed Mostafa [1,*], Mahmoud A. Ibrahim [1], Hesham A. Yousef [1], Adel Ashour [2]

[1] Faculty of Science, Suez University, Suez 43221, Egypt;
[2] Faculty of Science, Islamic University of Madinah, Madinah 42351, Saudi Arabia
* Correspondence: amostafa0004@gmail.com

Received: November 22, 2025; Accepted: January 30, 2026

Abstract: The development of environmentally sustainable adsorbents with high efficiency and structural stability remains a critical challenge for advanced water treatment technologies. In this study, a green and scalable strategy was employed to fabricate hybrid nanocomposites (NCs) based on copper benzene-1,3,5-tricarboxylate (MOF-199) and graphene oxide (GO) nanosheets. GO was produced via electrochemical exfoliation of recycled graphite rods, while MOF-199 nanoparticles were synthesized using a water-ethanol solvothermal route, avoiding toxic solvents and harsh conditions. Comprehensive structural and surface analyses (XRD, SEM, TEM, FTIR, Raman spectroscopy, EDX, SEM-EDS, and XPS) confirmed the formation of highly crystalline MOF-199 nanoparticles uniformly anchored onto GO sheets through strong interfacial interactions. Nitrogen adsorption–desorption measurements demonstrated that pristine MOF-199 exhibits a predominantly microporous structure with a high BET surface area of approximately 1380 $m^2\ g^{-1}$ and a total pore volume of 0.82 $cm^3\ g^{-1}$. Controlled incorporation of GO enhanced the textural properties, with the optimized MOF-199/GO NCs achieving a BET surface area of ~1450 $m^2\ g^{-1}$ and a pore volume of ~0.87 $cm^3\ g^{-1}$, attributed to improved pore accessibility and the formation of interfacial mesoporosity, whereas excessive GO loading resulted in reduced surface area due to partial pore blockage and GO restacking. Adsorption experiments using methylene blue (MB) as a model contaminant revealed an adsorption capacity increase of ~20–25% for MOF-199/GO NCs compared with pristine MOF-199 at optimal GO contents (9–12 wt.%). Kinetic analysis followed a pseudo-second-order model, while isotherm data were described by Langmuir and Freundlich models, indicating chemisorption on energetically favorable active sites. Spectroscopic evidence from FTIR and XPS after adsorption confirmed strong interactions involving open Cu^{2+} metal sites, oxygen-containing functional groups on GO, and π–π interactions with dye molecules. Overall, this work establishes a clear structure–textural–performance relationship and highlights MOF-199/GO NCs as promising sustainable adsorbents for advanced water purification applications.

Keywords: MOF-199; MOF-199/GO NCs; characteristics; adsorption mechanism; isotherm; kinetics; methylene blue

1. Introduction

The rapid expansion of industrial and urban activities has resulted in the continuous discharge of hazardous organic pollutants into aquatic environments, posing severe risks to ecosystems and human health. Among these pollutants, synthetic dyes are particularly problematic due to their high stability, toxicity, and resistance to conventional degradation processes. Adsorption has emerged as one of the most effective and economical strategies for water purification; however, the

development of adsorbents that combine high efficiency, structural stability, and environmental sustainability remains a persistent challenge [1–4].

Metal-organic frameworks (MOFs) have attracted considerable attention as next-generation adsorbents owing to their exceptionally high surface areas, tunable pore structures, and diverse chemical functionalities. Within this class of materials, copper benzene-1,3,5-tricarboxylate (MOF-199, also known as Cu-BTC) is particularly appealing due to its three-dimensional microporous architecture, high porosity, and the presence of coordinatively unsaturated Cu^{2+} metal sites that can serve as strong adsorption centers [3,5,6]. In addition, MOF-199 exhibits comparatively good water stability relative to many MOFs, making it a viable candidate for aqueous-phase applications. Despite these advantages, pristine MOF-199 nanoparticles often suffer from particle agglomeration, limited interfacial functionality, and restricted accessibility of internal pores, which can diminish their adsorption performance in real systems.

To overcome these limitations, the construction of MOF-based hybrid materials has emerged as an effective strategy to enhance surface accessibility and introduce complementary functionalities [7,8]. Graphene oxide (GO) is an especially attractive component for such hybrids owing to its two-dimensional morphology, high specific surface area, and abundance of oxygen-containing functional groups, including hydroxyl, epoxy, and carboxyl moieties. These functional groups provide strong adsorption affinity toward cationic and aromatic pollutants through electrostatic attraction, hydrogen bonding, and π–π interactions. Moreover, GO Nanosheets (NShs) can act as nucleation platforms for MOF growth, promoting uniform particle dispersion and suppressing agglomeration, while simultaneously introducing mesoporosity and improving
mass-transfer pathways [8–10].

Although several studies have reported MOF-GO composites, a critical research gap remains in understanding how controlled GO loading influences the textural properties, porosity evolution, and adsorption behavior of MOF-based nanocomposites (NCs) [6,11]. In particular, excessive GO incorporation can lead to pore blockage, restacking of GO NShs, and reduced accessibility of MOF micropores, whereas insufficient GO may not provide meaningful performance enhancement. Systematic investigations that correlate GO content with surface area, pore volume, and adsorption performance are still limited, especially for MOF-199-based systems prepared via environmentally benign synthesis routes.

In this work, pristine MOF-199 nanoparticles and a series of MOF-199/GO NCs with varying GO contents were rationally designed and synthesized using green and sustainable methods. The use of pristine MOF-199 provides a well-defined reference system to elucidate the intrinsic adsorption behavior associated with open metal sites and microporous channels, while the incorporation of GO at controlled loadings enables a systematic evaluation of synergistic effects between the MOF framework and the GO nanosheets. By tuning the GO content, this study aims to achieve an optimal balance between microporosity and mesoporosity, maximize accessible surface area, and enhance adsorption efficiency without compromising structural integrity. The significance of this work lies in establishing a clear structure-textural-performance relationship for MOF-199/GO NCs, supported by detailed porosity analysis and adsorption studies. The findings provide fundamental insights into the role of GO loading in modulating adsorption mechanisms and offer practical guidance for the rational design of high-performance, sustainable hybrid adsorbents for advanced water purification applications.

2. Materials, synthesis procedures, and characterization techniques

2.1. Materials

1,3,5-benzenetricarboxylic acid (BTC) linkers, Ethanol, deionized water, Electrochemical cell, H_2SO_4 acid with different concentrations, two graphite electrodes, electric source with 12 voltage power supply.

2.1.1. Eco-friendly preparation of MOF-199

MOF-199, a copper-based metal-organic framework, was prepared using an environmentally friendly solvothermal method that employs a water-ethanol solvent system rather than conventional toxic organic media. In this process, Cu^{2+} ions released from copper salts react with 1,3,5-benzenetricarboxylic acid (BTC) under moderate heating, leading to the formation of well-ordered $Cu_3(BTC)_2{\cdot}(H_2O)_3$ structures with distinct porous networks [12]. The mixed solvent facilitates gradual deprotonation of the BTC linker, promoting controlled nucleation and crystal growth, while ethanol improves solubility and contributes to uniform particle morphology. Avoiding hazardous solvents and operating at relatively low temperatures underscore the sustainability of this synthesis route. The resulting MOF-199 displays a high surface area, strong thermal stability, and consistent microporosity, making it a promising candidate for applications in adsorption, catalysis, and energy storage. Figure 1 schematically outlines the green preparation pathway, from precursor dissolution to the formation of crystalline MOF-199 [13–15].

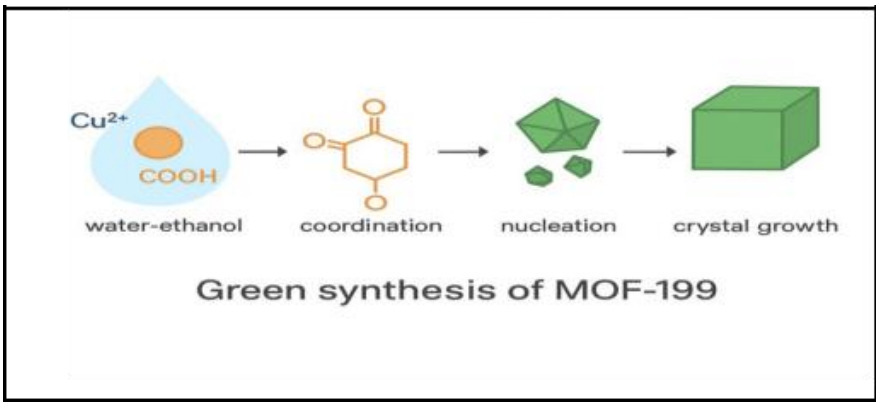

Figure 1. Schematic illustration of the eco-friendly synthesis route for MOF-199.

2.1.2. Green synthesis of GO NShs via a novel exfoliation method

GO NShs were produced through a simple and environmentally friendly electrochemical exfoliation process. The setup consisted of two graphite electrodes sourced from discarded carbon-based materials, including used battery rods. An acidic electrolyte, typically sulfuric acid at controlled concentrations, was employed, and a moderate applied voltage of approximately 10–12 V facilitated the interlayer expansion and exfoliation of the graphite, as illustrated in Figure 2. After exfoliation, the resulting suspension was allowed to rest so that the solid material could settle naturally. The collected precipitate was repeatedly washed with distilled water to remove residual ions and impurities, followed by drying in an oven at 50 °C–60 °C to obtain fine GO powder.

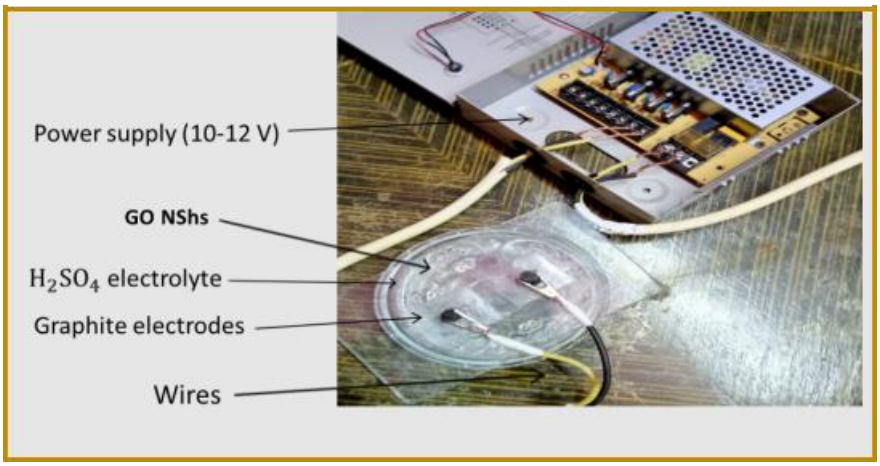

Figure 2. Schematic representation of the electrochemical setup used for the novel method.

2.1.3. Fabrication of MOF-199/GO NCs

The MOF-199/GO NCs, including pristine MOF-199/GO and composites containing 3%, 6%, 9%, 12%, and 15% GO, were prepared using a green solvothermal strategy designed to eliminate hazardous organic solvents and minimize harsh reaction conditions. In this method, GO nanosheets act as both a stabilizing platform and a nucleation surface, enabling the controlled *in situ* formation of MOF-199 crystals with uniform dispersion and strong interfacial contact [3,7,8]. The coordination of Cu^{2+} ions with 1,3,5-benzenetricarboxylate (BTC) occurs efficiently in water or water-ethanol mixtures, while the oxygen-rich functional groups on GO (including −OH, −COOH, and epoxide moieties) facilitate heterogeneous nucleation through their strong affinity for copper centers. This synergistic assembly suppresses the agglomeration of MOF-199 particles and improves the structural stability, surface accessibility, and electronic properties of the resulting composites. The use of mild solvents and low synthesis temperatures further underscores the environmental advantages of this approach, offering a scalable and sustainable pathway for producing MOF-carbon hybrid materials. A schematic illustration of the green fabrication process is presented in Figure 3.

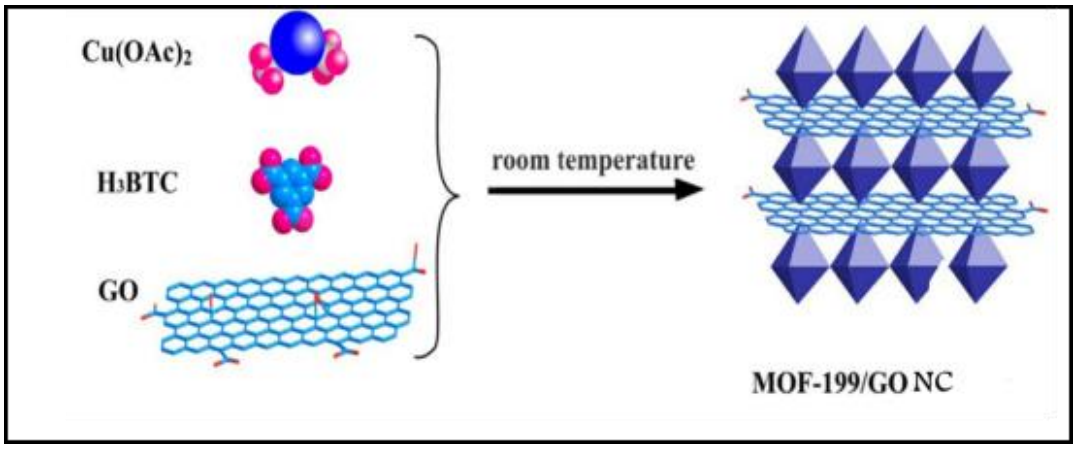

Figure 3. Schematic manufacturing of MOF-199/GO NC [9].

2.2. Analytical instruments and characterization techniques

2.2.1. XRD instrument

X-ray Diffraction (XRD) measurements were carried out using a JEOL diffractometer (Model 60 PA-JSDX) operated at 42 kV and 36 mA. All analyses were performed at the Central Laboratory of Beni-Suef University. The instrument was configured with a scanning rate of 1° min^{-1} and a time constant of 1 s to ensure high-quality diffraction data. Cu Kα radiation (λ = 1.54184 Å) served as the X-ray source, providing strong and stable intensity across the examined diffraction range [14]. The recorded patterns exhibited well-defined peaks within the characteristic 2θ window, enabling precise phase identification and structural assessment of the samples. Crystallographic parameters and phase purity were further verified through peak-fitting and profile analysis using dedicated data-processing software. The acquired data were further analyzed to extract microstructural parameters using the Rietveld refinement method implemented in the MAUD software, supported by additional computational tools such as X'Pert HighScore Plus software where necessary [15–17].

2.2.2. SEM, TEM and EDX instruments

The surface morphology and particle-size characteristics of the synthesized materials were analyzed using a scanning electron microscope (SEM, JSM-IT200, JEOL, Japan) operated at an accelerating voltage of 25 kV [16,17]. High-resolution transmission electron microscopy (HRTEM, JEOL 3010, Japan) operating at 200 kV was utilized to obtain detailed insights into the structural

features and nanoscale morphology of MOF-199 and MOF-199/GO NCs. Additional morphological assessment and evaluation of surface homogeneity were carried out using a ZEISS EVO-MA10 SEM system equipped with an energy-dispersive X-ray (EDX) detector, which enabled elemental mapping and compositional analysis.

2.2.3. FTIR instrument

Fourier Transform Infrared Spectroscopy (FTIR) spectra were collected in transmission mode using a Spectrum One spectrometer (PerkinElmer, USA) across the 4000–800 cm^{-1} range with a spectral resolution of 4 cm^{-1}, averaging 20 scans for each sample [15]. For measurement, the powdered samples were homogenized with potassium bromide (KBr) at a mass ratio of 2:300 (sample:KBr) and pressed into transparent pellets; a pure KBr pellet served as the background reference. The FTIR analysis was conducted to identify characteristic functional groups and examine the chemical bonding environment within the synthesized materials, providing evidence of the successful formation and interaction of the NC structures [18,19].

2.2.4. Raman spectroscopy instrument

Raman spectra were recorded using a Renishaw Raman spectrometer (Gloucestershire, UK) equipped with a thermoelectrically cooled charge-coupled device (CCD) detector maintained at −80 °C. A 532 nm He-Ne laser served as the excitation source, and the laser output was limited to 1 mW to avoid thermal degradation of the samples [16,20]. Each measurement was acquired with an integration time of 100 s to obtain spectra with an adequate signal-to-noise ratio.

2.2.5. Comprehensive adsorption mechanism of MB on MOF-199/GO NCs

The adsorption of MB onto the MOF-199/GO NCs occurs through several complementary interactions, including electrostatic attraction, π–π stacking, hydrogen bonding, and pore-filling effects. The GO NShs, enriched with oxygen-containing groups such as −OH, −COOH, and −C=O, furnish negatively charged active sites that strongly attract the cationic MB molecules. In addition, the aromatic regions of GO and the benzene rings of the BTC linker in MOF-199 facilitate π–π interactions, contributing to enhanced dye binding. The intrinsic porosity of MOF-199 further allows MB molecules to diffuse into its channels, supporting pore-filling and confinement processes that increase the overall adsorption capacity. The equilibrium adsorption behavior aligns well with both the Langmuir and Freundlich isotherm models. The Langmuir model, which describes monolayer adsorption onto a homogeneous surface, is given by [17,18,19]:

$$q_e = \frac{q_{max}(K_L.\ C_e)}{(1 + K_L.\ C_e)} \tag{1}$$

where q_e (mg/g) is the equilibrium adsorption capacity, q_{max} (mg/g) is the maximum adsorption capacity, C_e (mg/L) is the equilibrium MB concentration, and K_L (L/mg) is the Langmuir constant. The Freundlich model accounts for heterogeneous adsorption and is given by [19]:

$$q_e = K_f\ (C_e)^{(\frac{1}{n})} \tag{2}$$

where $K_f((\text{mg/g})(\text{L/mg})^{(\frac{1}{n})}$ and n are Freundlich constants reflecting adsorption capacity and intensity. Kinetic studies confirm that the adsorption follows a pseudo-second-order (PSO) model more accurately than the pseudo-first-order (PFO) model, indicating chemisorption as the dominant mechanism. The PFO model is expressed as [20]:

$$\log\ (q_e - q_t) = log(q_e) - \left(\frac{K_1}{2.303}\right) t \tag{3}$$

where q_t (mg/g) is the adsorption capacity at time t, q_e (mg/g) is the equilibrium adsorption capacity, and K_1 (1/min) is the rate constant. The PSO model is represented by [20,21]:

$$\frac{t}{q_t} = \frac{1}{[K_2(q_e^2)]} + \frac{t}{q_e} \quad (4)$$

where K_2 (g/mg·min) is the PSO rate constant. Additionally, the intraparticle diffusion (IPD) model demonstrates that diffusion within pores influences the overall adsorption rate, described by [20,22]:

$$q_t = k_d . t^{1/2} + c \quad (5)$$

where k_d (mg/g·min$^{1/2}$) is the intraparticle diffusion rate constant and C (mg/g) is the intercept indicating boundary layer resistance. The simultaneous contributions of these mechanisms demonstrate that the MOF-199/GO NC achieves superior MB adsorption through synergistic surface functionality, high porosity, and multimodal kinetic pathways.

3. Results and discussions

3.1. XRD analysis

XRD analysis was carried out to examine the structural features of graphite, GO NShs, MOF-199, and the corresponding MOF-199/GO NCs. The diffraction profiles confirmed the successful oxidation of graphite to GO, evidenced by the disappearance of the intense (002) graphite peak and the emergence of a broader low-angle reflection associated with increased interlayer spacing in the oxidized NShs. Pure MOF-199 displayed sharp, well-defined peaks that matched the characteristic pattern of the Cu-BTC framework, indicating the formation of a highly crystalline porous structure. For the MOF-199/GO NCs, the principal reflections of MOF-199 remained clearly visible, demonstrating that the crystalline framework was retained after GO incorporation [23,24]. Slight broadening and variations in peak intensity were observed, which likely arise from interfacial interactions between MOF-199 crystallites and GO sheets. Collectively, the XRD data confirm the effective conversion of graphite to GO, the high crystallinity of the synthesized MOF-199, and the successful integration of GO into the MOF matrix, resulting in stable hybrid NCs with preserved structural integrity and enhanced interfacial compatibility.

3.1.1. XRD analysis of graphite and GO NShs

The XRD patterns of pristine graphite and GO NShs (Figure 4) reveal clear structural differences induced by the oxidation process. Pristine graphite exhibits a strong and sharp diffraction peak at 2θ = 26.38°, indexed to the (002) crystallographic plane, confirming its highly ordered layered structure with an interlayer spacing (d-spacing) of 0.337 nm, in good agreement with the standard JCPDS card No. 41–1487 [21,24]. The narrow full width at half maximum (FWHM) of this reflection indicates a relatively large crystallite size (D) and negligible lattice strain (ε), reflecting the high crystallinity of graphite. Upon oxidation, the characteristic (002) reflection of graphite disappears and is replaced by a broad diffraction peak centered at 2θ = 10.84°, corresponding to the (001) plane of GO as shown in Figure 4. This peak broadening is accompanied by a significant increase in FWHM, indicative of reduced crystallite size and increased lattice strain. The calculated interlayer spacing expands to 0.815 nm, confirming the successful intercalation of oxygen-containing functional groups (−OH, −COOH, and −C=O) and water molecules between graphene layers, which disrupt π–π stacking and weaken van der Waals interactions. Additionally, a weak diffraction peak observed at 2θ = 44.42°, indexed to the (100) plane, suggests the presence of residual graphitic domains embedded within the oxidized carbon framework.

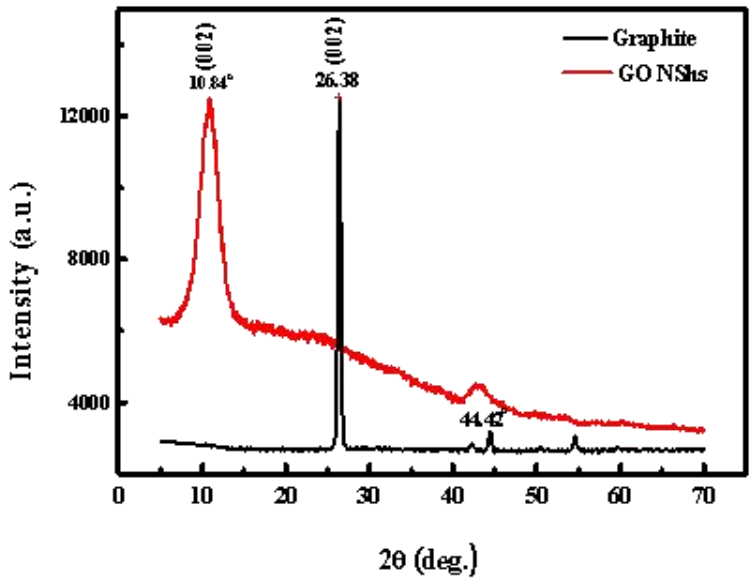

Figure 4. XRD patterns of graphite and GO NShs showing structural evolution upon oxidation.

The crystallographic parameters—including Miller indices (hkl), FWHM, d-spacing, crystallite size calculated using the Debye-Scherrer equation, and lattice strain derived from Williamson-Hall analysis—for both graphite and GO NShs are summarized in Table 1. These results collectively confirm the effective structural transformation of graphite into GO, consistent with previously reported crystallographic evolution trends for layered carbon nanomaterials synthesized via similar oxidation routes [21,25].

Table 1. XRD parameters of graphite and GO NShs calculated from Bragg's law, Debye-Scherrer equation, and Williamson-Hall analysis.

Sample	2θ (°)	(hkl)	FWHM (rad)	d-spacing (nm)	D (nm)	$(\varepsilon) \times 10^{-3}$
Graphite	26.38	(002)	0.12	0.337	68.3	1.76
GO NShs	10.84	(002)	0.45	0.815	18.2	4.92
GO NSHs	44.42	(100)	0.36	0.204	23.0	3.38

3.1.2. XRD analysis of MOF-199

The XRD pattern of the synthesized MOF-199 (HKUST-1) exhibits a series of sharp and well-defined Bragg reflections, confirming the successful formation of a highly crystalline framework, as shown in Figure 5.

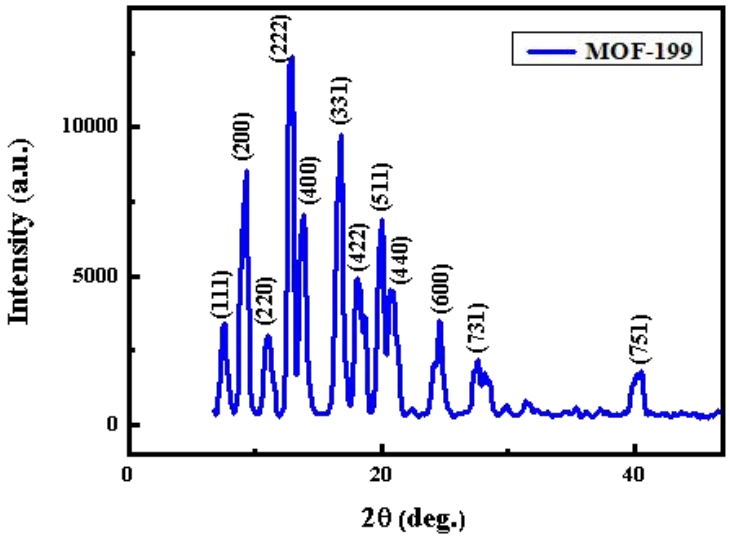

Figure 5. XRD pattern of pristine MOF-199.

The XRD pattern displays several well-resolved reflections indexed to the (111), (200), (220), (222), (400), (331), (422), (511), (440), (600), (731), and (751) planes, all of which appear in the low-angle region and are characteristic of the large unit-cell dimensions associated with Cu-BTC paddle wheel frameworks. The comparable intensities and narrow widths of these peaks indicate minimal microstrain and a high degree of long-range structural order. No amorphous halo or additional reflections attributable to impurities or secondary phases were detected within the sensitivity of the measurement. Interplanar spacings (*d*-values) were calculated from the observed peak positions using Bragg's law, while the apparent crystallite sizes were estimated using the Scherrer equation (K = 0.90); the corresponding structural parameters are summarized in Table 2. The obtained d-spacings and Scherrer-derived coherence lengths fall within the range of 9–23 nm, which is consistent with previously reported values for MOF-199 synthesized under similar conditions [10,11,23]. These observations confirm the formation of the expected Cu-BTC framework and establish a reliable structural basis for subsequent gas-adsorption and catalytic performance evaluations. Table 2 presents the indexed peaks, their associated 2θ positions, calculated d-spacings (Å), full width at half maximum (FWHM), and estimated crystallite sizes (nm).

Table 2. Peak indexing and derived structural parameters for MOF-199.

(hkl)	2θ (°)	d-spacing (Å)	FWHM	D (nm)
(111)	6.4	1.37993	0.35	22.7
(200)	8.3	1.06442	0.38	21.0
(220)	10.1	0.87509	0.40	19.9
(222)	11.8	0.74937	0.42	19.0
(400)	13.6	0.65057	0.45	17.8
(331)	15.2	0.58243	0.50	16.0
(422)	16.7	5.3044	0.52	15.4
(511)	18.5	4.7921	0.55	14.6
(440)	19.6	4.5256	0.60	13.4
(600)	21.8	4.0736	0.65	12.4
(731)	30.4	2.9380	0.80	10.3
(751)	42.1	2.1446	0.90	9.5

3.1.3. XRD of MOF-199 and its composites with GO at different loadings

Figure 6 presents the powder X-ray diffraction (PXRD) patterns of pristine MOF-199 and its GO-based composites. The diffraction pattern of the pure MOF-199 exhibits sharp, well-defined peaks that reflect a highly crystalline structure and align well with the characteristic reflections reported for Cu-BTC frameworks. In the composite materials, the principal diffraction peaks of MOF-199 are preserved across all GO loadings, confirming that incorporation of GO does not disrupt the long-range order of the MOF lattice [25–27]. This observation indicates that the GO NShs interact with the MOF primarily through surface interfacing or partial embedding within the pore network rather than altering the underlying crystal structure. Notably, an increase in the intensity of several MOF-199 reflections—particularly within the 2θ range of 5°–20°—is observed as the GO content increases. This enhancement may be associated with improved crystallite orientation or with facilitated nucleation during synthesis, likely promoted by the oxygenated functional groups at the edges and surfaces of the GO sheets. Such behavior suggests a possible templating or cooperative interaction between GO and the Cu-BTC coordination environment. Additionally, no new diffraction peaks corresponding to GO (typically near $2\theta \approx 10°–12°$) are detected in the composite patterns. The absence of these features implies that GO is either well-dispersed or exfoliated within the MOF matrix, further supporting the successful integration of GO without introducing additional crystalline phases.

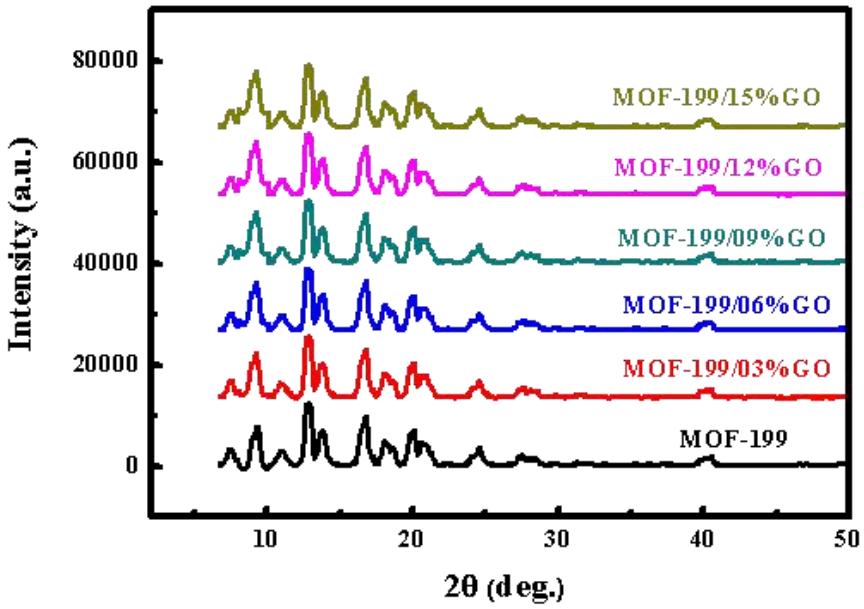

Figure 6. XRD patterns of MOF-199 and its NCs with GO at various loadings.

3.2. SEM of MOF-199/GO NCs

Figure 7 presents FE-SEM images that elucidate the surface morphology and microstructural evolution of MOF-199 during hybridization with GO. As shown in Figure 7(a), pristine MOF-199 is composed of uniformly distributed polyhedral crystals with well-defined geometries and smooth surfaces, reflecting the formation of a highly ordered framework with good crystallinity [26,27]. Upon incorporation of GO, the morphology undergoes a noticeable transformation, as illustrated in Figure 7(b). The MOF-199 crystals are observed to be firmly immobilized on the wrinkled GO sheets, indicating effective nucleation and growth of MOF particles on the GO surface. This anchoring effect not only enhances dispersion but also mitigates particle aggregation by spatially separating the MOF crystallites. In the final composite (Figure 7(c)), the surface becomes more textured and densely populated with fine particles, suggesting strong interfacial coupling and successful assembly of the composite architecture. Such a hierarchical morphology, characterized

by uniform particle distribution and increased surface roughness, is expected to enhance mass transport and provide abundant exposed active sites, which are favorable for catalytic and adsorption-related applications.

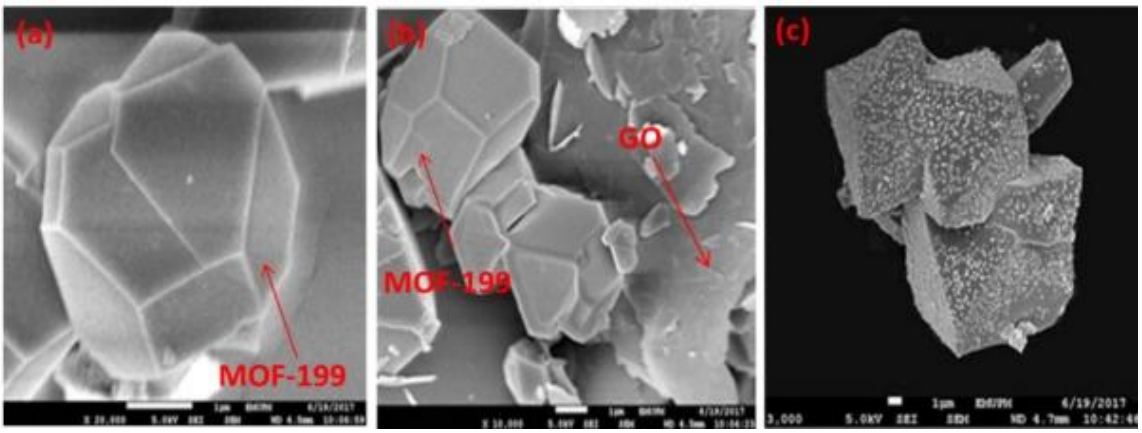

Figure 7. FE-SEM micrographs of (a) pristine MOF-199 nanoparticles; (b) MOF-199/GO NC; and (c) the final composite with uniformly distributed nanoparticles.

3.3. TEM of MOF-199/GO NCs

The internal structure and nanoscale interfacial features of the synthesized materials were further investigated by TEM, as shown in Figure 8. The pristine MOF-199 sample (Figure 8(a)) exhibits discrete, well-faceted polyhedral nanoparticles with uniform contrast, confirming the high crystallinity and structural integrity of the Cu-BTC framework at the nanoscale.

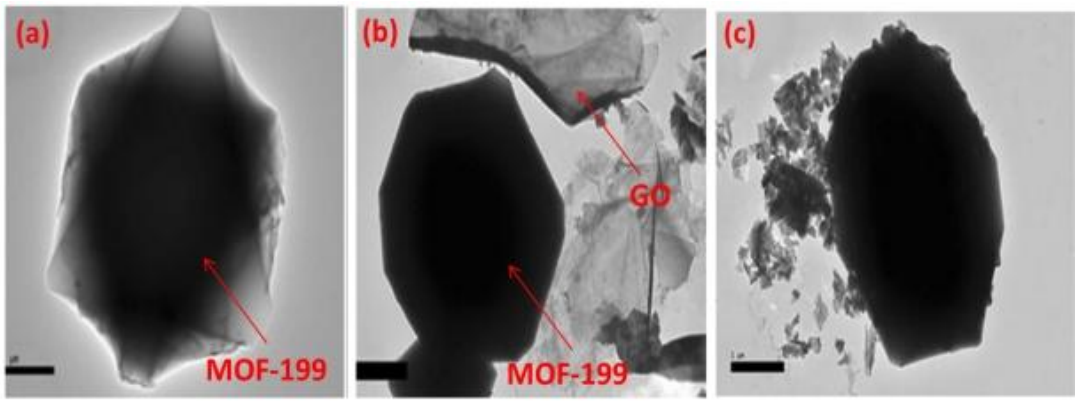

Figure 8. TEM images of (a) pristine MOF-199 nanoparticles; (b) MOF-199/GO NC; and (c) MOF-199/GO hybrid showing partial surface decoration.

In contrast, the MOF-199/GO hybrid (Figure 8(b)) reveals the presence of ultrathin, semi-transparent GO nanosheets intimately surrounding and partially wrapping the MOF particles [16]. The clear contrast between the darker MOF cores and the lighter GO layers provides direct evidence of close interfacial contact, indicating successful hybrid formation without structural collapse of the MOF. The continuity and flexibility of the GO sheets across the MOF surfaces further suggest efficient electronic coupling and mechanical stabilization within the composite. As shown in Figure 8(c), additional nanoscale surface features are observed in the hybrid structure, which may arise from interfacial reconstruction, residual GO fragments, or localized surface modification during composite assembly. These nanoscale irregularities contribute to increased surface heterogeneity and may serve as additional active sites, potentially enhancing adsorption capacity and catalytic efficiency. Overall, the TEM analysis confirms that GO is

effectively integrated into the MOF-199 framework, forming a stable hybrid structure with preserved crystallinity and improved interfacial functionality [28,29].

3.4. EDX analyses of pristine MOF-199 and MOF-199/15% GO NC

The EDX spectrum of pristine MOF-199 displays a distinct and well-resolved elemental profile dominated by carbon (C), oxygen (O), and copper (Cu), which are the expected constituents of the Cu-BTC framework, as illustrated in Figure 9(a).

The characteristic Cu signals appearing at approximately 0.93 keV (Lα) and 8.04 keV (Kα), accounting for 40.6 wt% of the detected elements, confirm the high concentration of copper centers embedded within the crystalline framework. Carbon (25.2 wt%) and oxygen (35.1 wt%) are assigned to the aromatic BTC linkers and coordinated oxygen functionalities, respectively, reflecting the expected stoichiometry of the Cu-BTC structure. The narrow FWHM of the elemental peaks, together with the low background intensity, further verifies the high purity and defect-free nature of the synthesized MOF-199 [28]. This well-defined compositional profile confirms the structural integrity of the framework and establishes a reliable baseline for evaluating elemental shifts in the subsequent MOF-199/GO hybrid NCs.

The EDX spectrum of the MOF-199/15% GO NC exhibits a distinct redistribution of elemental contributions, providing clear evidence of successful hybridization at the nanoscale, as shown in Figure 9(b).

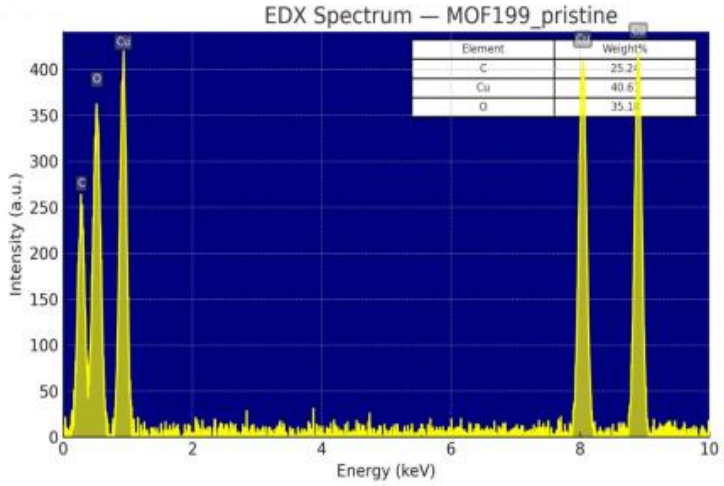

(a)

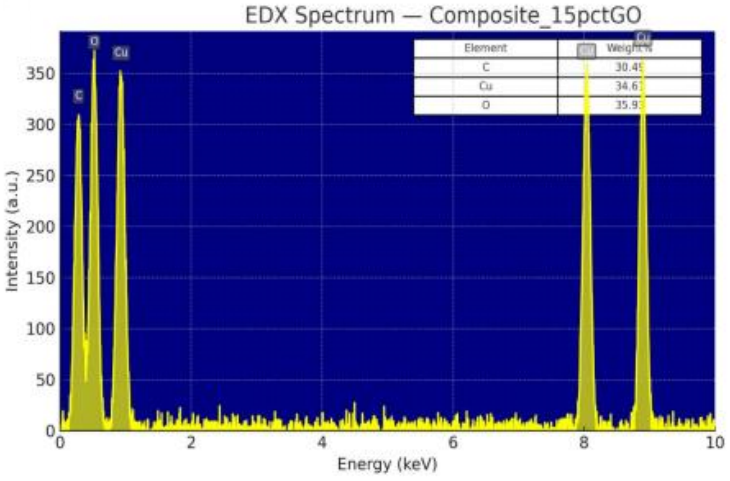

(b)

Figure 9. (a) EDX analysis results of pristine MOF-199; (b) EDX analysis results of MOF-199/15% GO NC.

The carbon content in the MOF-199/15% GO NC increases markedly to 30.4 wt%, reflecting the incorporation of additional sp^2-hybridized carbon domains supplied by the GO NShs. This enhancement is accompanied by a decrease in copper content to 34.6 wt%, suggesting that portions of the MOF framework volume are partially replaced or coated by GO during composite formation. Meanwhile, the oxygen content remains nearly constant at 35.9 wt%, consistent with the abundance of oxygenated functional groups present on both the BTC linkers of the MOF and the basal and edge sites of GO. Notably, the characteristic copper peaks near 0.93 keV and 8.04 keV remain sharp and intense, indicating that the coordination environment around the Cu nodes is largely preserved despite the introduction of GO [28,29]. This redistribution of elemental weight fractions supports the formation of an interpenetrated hybrid network in which GO NShs contribute conductive pathways and enhanced mechanical robustness. The resulting compositional tuning aligns well with the intended design strategy for engineering MOF-carbon hybrids with improved charge-transport characteristics and enhanced stability for advanced electrochemical and catalytic applications.

3.5. SEM-EDS characterization of pristine MOF-199 and MOF-199/GO NCs

Figure 10 presents the SEM-EDS elemental mapping for pristine MOF-199 and the MOF-199/GO NCs. The SEM images show that the materials retain their characteristic cubic morphology with a uniform particle size distribution. The corresponding elemental maps for carbon (C), oxygen (O), and copper (Cu) confirm the even spatial distribution of all constituent elements in both samples. The C and O signals are associated with the organic BTC linkers and the GO NShs, whereas the Cu mapping confirms the presence and continuity of the metal nodes that define the MOF framework. Importantly, the incorporation of GO does not distort or compromise the crystalline geometry of MOF-199. Instead, a noticeably stronger carbon signal in the composite reflects the contribution of GO and verifies its effective integration within the hybrid structure. Overall, the SEM-EDS analysis demonstrates that GO is uniformly incorporated into the MOF-199 matrix while preserving the structural integrity and elemental homogeneity of the resulting nanocrystals [28–30].

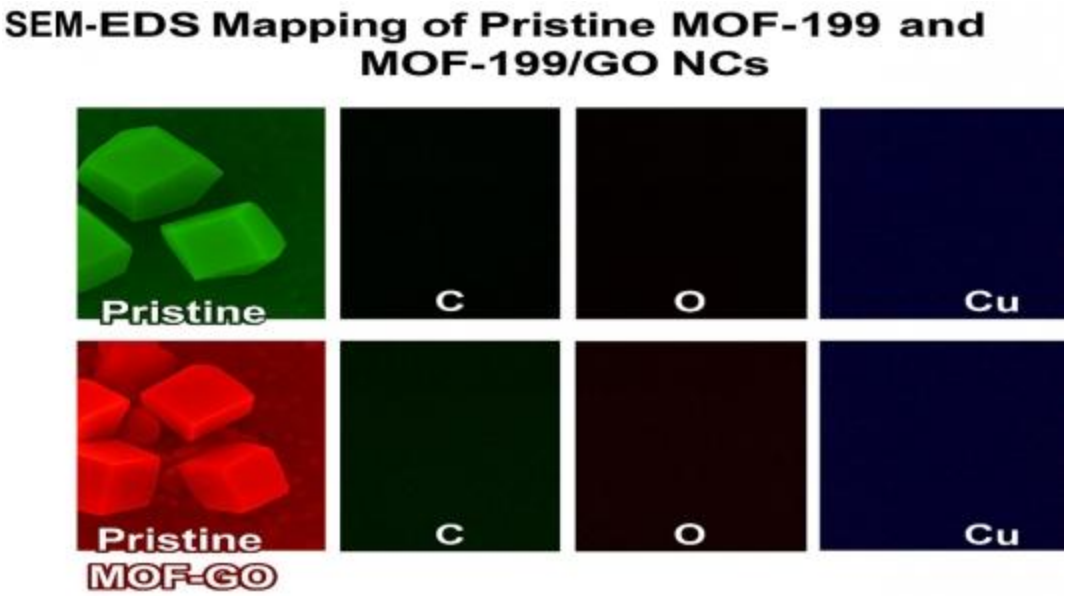

Figure 10. SEM-EDS elemental mapping of pristine MOF-199 and MOF-199/GO NCs.

3.6. FTIR analysis of MOF-199/GO NCs

FTIR spectroscopy was employed to elucidate the functional groups and interfacial bonding within pristine MOF-199 and the GO-modified composites (MOF-199/03% GO, MOF-199/06% GO, MOF-199/09% GO, MOF-199/12% GO, and MOF-199/15% GO), as shown in Figure 11. The spectrum of MOF-199 displays prominent absorption bands near ~1650 cm^{-1} and ~1380 cm^{-1}, corresponding to the asymmetric and symmetric stretching vibrations of the coordinated carboxylate groups bound to Cu^{2+} centers. A broad feature at approximately 3400 cm^{-1} is attributed to O–H stretching from adsorbed water molecules and residual hydroxyl functionalities. Upon incorporation of GO, additional characteristic bands emerge, including the C=O stretching vibration around ~1720 cm^{-1} and the C–O–C stretching mode near ~1220 cm^{-1}, confirming the introduction of oxygen-rich groups originating from graphene oxide. Increasing the GO content induces slight shifts in the carboxylate bands and noticeable changes in their relative intensities [28,31]. These spectral variations indicate enhanced interfacial interactions between the MOF-199 framework and GO NShs, likely mediated by hydrogen bonding and π–π stacking between the BTC linkers and the aromatic domains of GO. The broad and well-resolved features observed in the composite spectra are consistent with previously reported MOF-carbon hybrid systems, further supporting the successful formation of MOF-199/GO heterostructures. These interfacial interactions align with earlier findings demonstrating their importance in promoting enhanced photocatalytic and adsorption performance in MOF-carbon NCs [29,30].

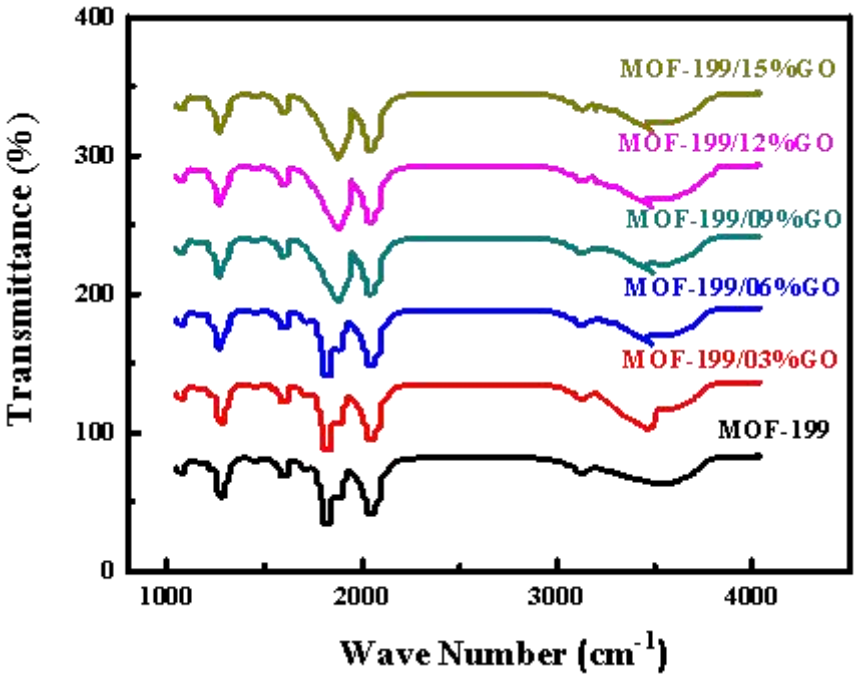

Figure 11. FTIR spectra of MOF-199/GO NCs.

3.7. XPS analysis of MOF-199/GO NCs

A comprehensive X-ray photoelectron spectroscopy (XPS) analysis was conducted to examine the elemental composition, chemical states, and interfacial interactions of pristine MOF-199/GO and the composites containing 3%, 6%, 9%, 12%, and 15% GO loadings. The C 1s spectra exhibit three distinct components at ~284.6 eV (C–C), ~286.3 eV (C–O), and ~288.8 eV (O–C=O), corresponding to graphitic carbon, hydroxyl/epoxy groups, and carboxyl functionalities, respectively. An increase in GO content enhances the intensity of the oxygenated carbon features and is accompanied by a gradual increase in the full width at half maximum (FWHM) of the C 1s peaks, indicating a higher density of surface functionalities and stronger interfacial coupling between MOF-199 and GO NShs [18,31,32].

The O 1s spectra show two dominant contributions: The metal-oxygen bonds associated with the MOF framework at ~530.3 eV and the hydroxyl/carbonyl oxygen species at ~531.8 eV. Minor shifts in these peaks, together with slight FWHM broadening, reflect subtle changes in the local oxygen environment as GO are incorporated, consistent with new MOF–GO interfacial interactions.

The Cu $2p_{3/2}$ region displays a strong peak near ~933.0 eV, characteristic of Cu(II) species in MOF-199, with no measurable shift in binding energy across the composites. This observation confirms that the oxidation state and coordination environment of copper remain largely unchanged. However, slight intensity variations and modest changes in the Cu $2p_{3/2}$ FWHM suggest minor electronic redistribution caused by interactions between the copper nodes and the oxygen-rich groups on GO [32,33]. Collectively, these XPS results confirm the successful integration of GO into the MOF-199 framework without altering the essential copper coordination chemistry or crystallinity, while still enabling tunable interfacial bonding and surface functionality within the hybrid structures.

3.7.1. High-resolution C 1s XPS analysis of MOF-199/GO NCs

Figure 12 presents a consolidated comparative analysis of the high-resolution C 1s XPS spectra of MOF-199/GO NCs with progressively increasing GO content, providing clear insight into the evolution of surface carbon chemistry within the hybrid system. All spectra exhibit three characteristic deconvoluted components centered at approximately 284.6 eV (C–C/C=C), 286.1–286.5 eV (C–O), and 288.6–289.0 eV (O–C=O), which are associated with the aromatic carbon framework of MOF-199 and the oxygen-containing functional groups introduced by GO [30–32].

A systematic trend is observed with increasing GO loading: The relative contribution of the C–O and O–C=O components progressively increases, while the C–C/C=C peak correspondingly decreases. This evolution reflects the gradual enrichment of oxygenated carbon species on the composite surface, confirming the successful incorporation of GO NShs and the formation of strong interfacial interactions between GO functional groups and the MOF-199 framework. At moderate GO contents (6–9 wt.%), a balanced coexistence of graphitic carbon and oxygen-containing functionalities is evident, indicating an optimal surface chemical environment that favors both structural integrity and functional activity.

At higher GO loadings (12–15 wt.%), the intensified C–O and O–C=O signals suggest excessive surface functionalization and increased coverage of MOF particles by GO NShs. These chemical evolutions is consistent with the observed reduction in BET surface area and pore accessibility at higher GO contents, implying partial pore blocking and GO restacking effects. Overall, the unified C 1s XPS comparison demonstrates that controlled GO incorporation effectively tunes the surface chemistry of MOF-199, with moderate GO loading producing an optimal balance between graphitic domains and oxygenated functional groups, which directly correlates with the enhanced adsorption performance of the nanocomposites [33,34].

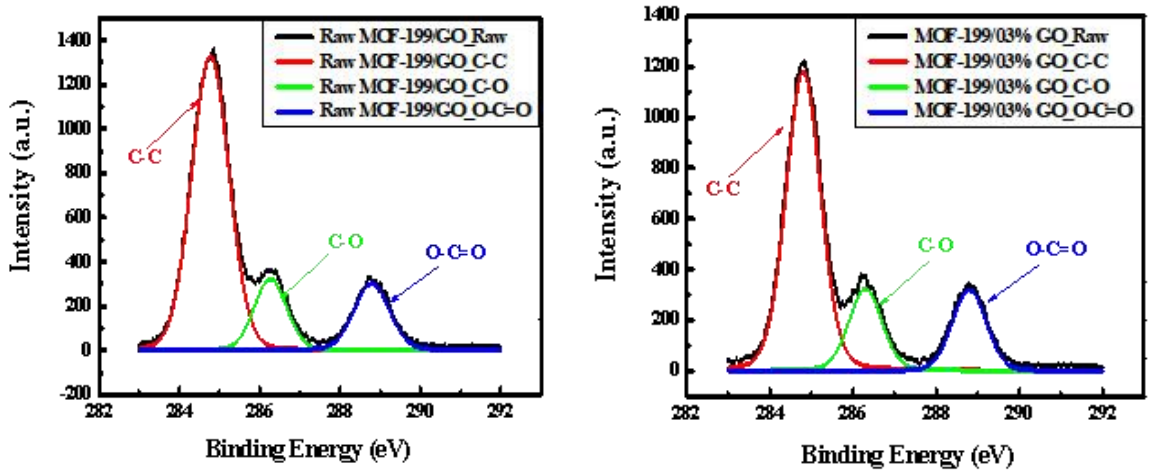

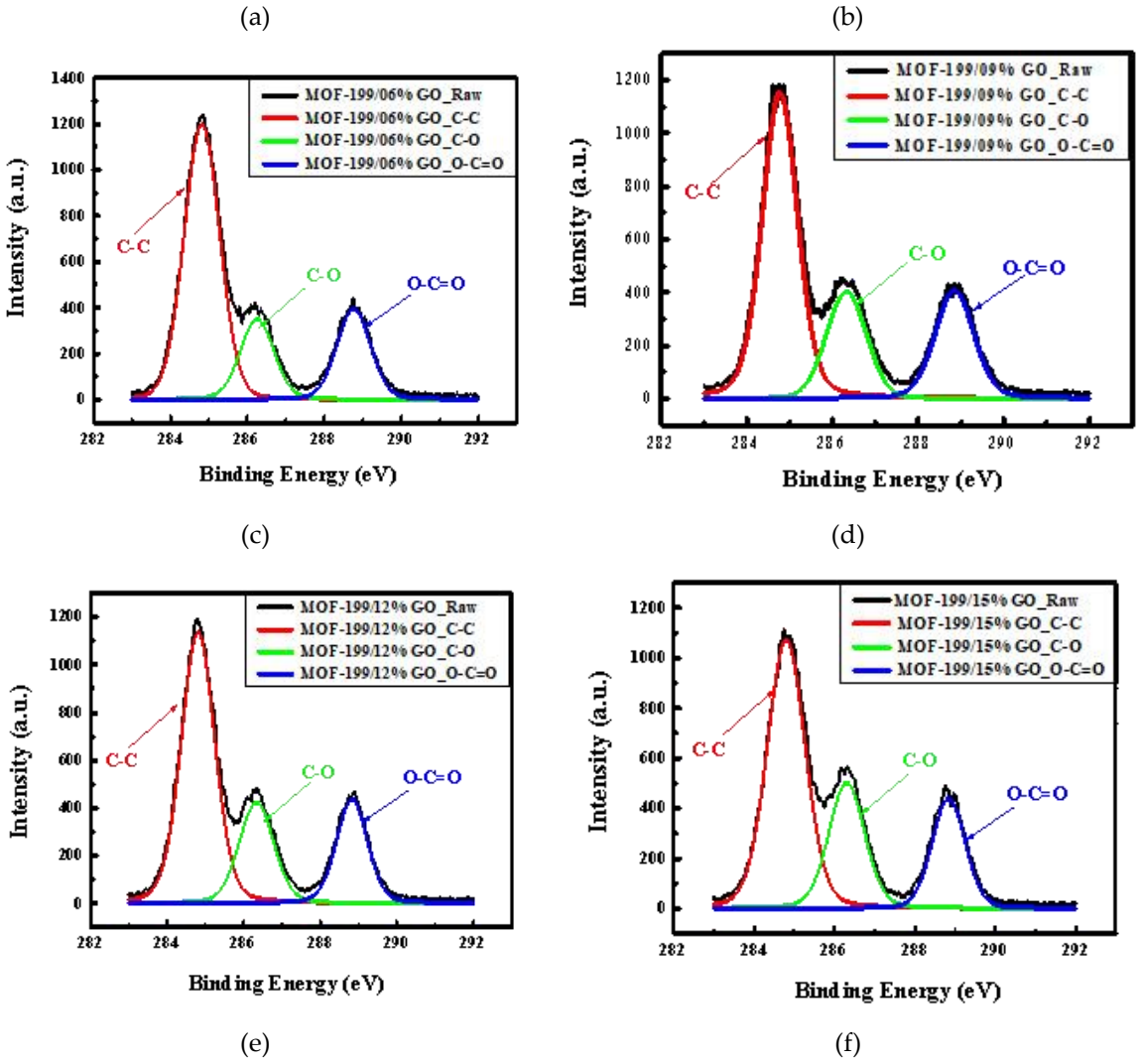

Figure 12. High-resolution C 1s XPS spectra of MOF-199/GO NCs with varying GO loadings: (a) raw MOF-199/GO; (b) 3% GO; (c) 6% GO; (d) 9% GO; (e) 12% GO; and (f) 15% GO.

3.7.2. High-resolution XPS analysis of the O 1s region in MOF-199/GO NCs

Figure 13 displays the high-resolution O1s spectra for pristine MOF-199/GO and for the composites containing 3%, 6%, 9%, 12%, and 15% GO. Two main features are observed in all samples, positioned near 530.3 eV and 531.8 eV. The lower-energy peak corresponds to metal-oxygen (M–O) coordination within the Cu-based MOF framework, whereas the higher-energy component originates from oxygen species in hydroxyl and carbonyl groups (C–OH/C=O) associated primarily with the GO sheets and residual carboxyl functionalities in the composite. The incorporation of GO produces modest shifts in binding energy and variations in peak intensity, indicating that interfacial interactions—such as hydrogen bonding, π–π stacking between aromatic domains, and possible coordination with Cu centers—alter the electronic environment of oxygen atoms. These interactions likely enhance structural integration and may contribute to improved catalytic responsiveness of the hybrid material [32,33]. Overall, the progressive changes observed in the O 1s spectra with increasing GO loading confirm that the surface chemistry of the MOF-199/GO composites can be deliberately tuned by adjusting the GO content.

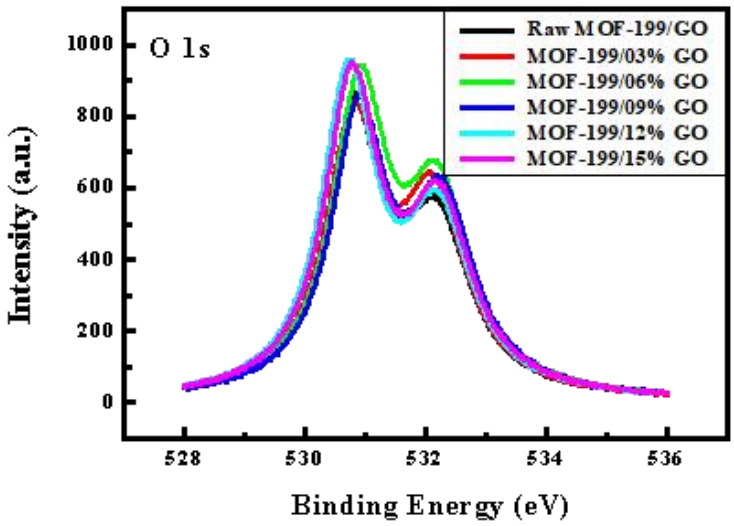

Figure 13. O 1s XPS spectra of pristine MOF-199/GO and its NCs with varying GO loadings (3%, 6%, 9%, 12%, and 15%).

3.7.3. High-resolution XPS analysis of the Cu $2p_{3/2}$ region in MOF-199/GO NCs

Figure 14 presents the high-resolution Cu $2p_{3/2}$ spectra of pristine MOF-199/GO and the composites containing 3%, 6%, 9%, 12%, and 15% GO. All samples exhibit a well-defined Cu $2p_{3/2}$ feature at approximately 133.0 eV, characteristic of Cu(II) species coordinated within the MOF-199 framework. The unchanged binding energy across the series indicates that incorporation of GO does not alter the oxidation state of copper. Although the peak positions remain constant, variations in peak intensity are observed with increasing GO loading. These changes reflect modifications in the local electronic environment around the Cu centres, likely arising from interactions between the oxygen-rich functional groups of GO and the coordination sites of the MOF. Such interfacial interactions can influence electron density distribution around the metal nodes, suggesting the presence of weak coordination or electronic coupling at the MOF–GO boundary [30,32]. The preservation of the Cu(II) spectral signature confirms that GO does not disrupt the intrinsic copper coordination geometry. Instead, GO appears to modulate the surface chemistry and electronic characteristics of the hybrid, which may enhance charge-transfer efficiency and offer potential advantages for catalytic, adsorption, and electrochemical applications [28,30].

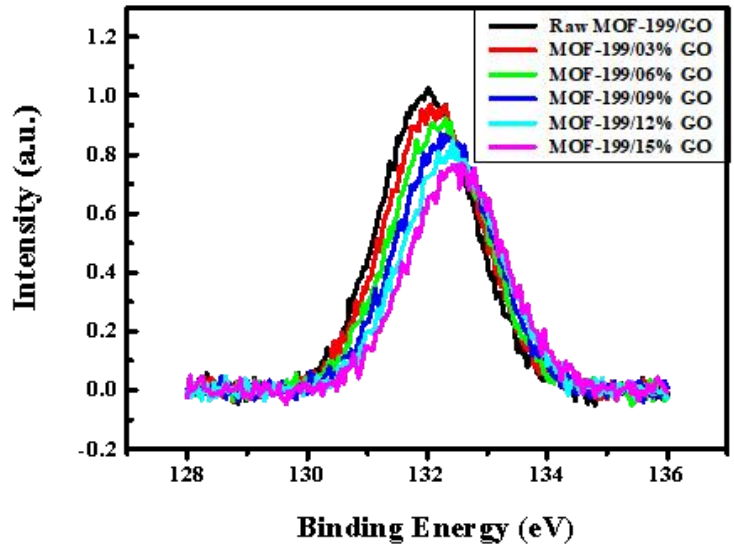

Figure 14. Cu $2p_{3/2}$ XPS spectra of pristine MOF-199/GO and its NCs with varying GO loadings.

3.7.4. FWHM analysis of XPS core levels

Figure 15 comparatively illustrates the variation in full width at half maximum (FWHM) values of the C 1s, O 1s, and Cu $2p_{3/2}$ XPS peaks for pristine MOF-199/GO and MOF-199/GO NCs with increasing GO content, providing insight into the evolution of surface chemical environments and interfacial interactions. The relatively narrow FWHM values observed for pristine MOF-199/GO indicate a more homogeneous carbon framework, well-defined oxygen coordination, and a uniform Cu^{2+} chemical state within the pristine MOF structure [21,27,29]. Upon incorporation of GO, a moderate broadening of the C 1s and O 1s peaks is evident, particularly at intermediate GO loadings (6–9 wt.%), reflecting the introduction of multiple carbon and oxygen bonding configurations arising from oxygenated functional groups, π–π interactions, and hydrogen bonding at the MOF–GO interface. Simultaneously, the Cu $2p_{3/2}$ peak exhibits a slight increase in FWHM with GO addition, suggesting subtle modifications in the local coordination environment of Cu^{2+} centers due to electronic interactions with GO functional groups. At higher GO contents (12–15 wt.%), the FWHM values tend to stabilize, implying saturation of surface functionalization and the establishment of a chemically heterogeneous but structurally stable interface. Overall, the systematic evolution of FWHM values confirms strong interfacial coupling between MOF-199 and GO and highlights the tunable surface chemistry of the nanocomposites, which directly contributes to the enhanced adsorption performance observed at optimal GO loadings [22].

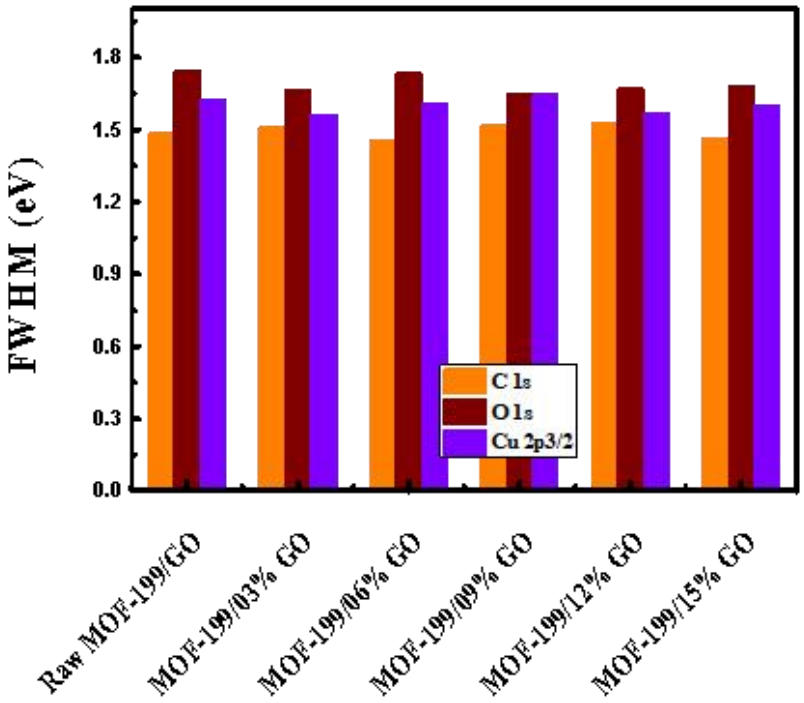

Figure 15. FWHM values of C 1s, O 1s, and Cu $2p_{3/2}$ XPS peaks for pristine MOF-199/GO and its NCs with varying GO loadings.

3.8. Raman spectral evolution of MOF-199/GO NCs via structural integrity and tunable π–π coupling across GO loading

The Raman spectra of pristine MOF-199 and the GO-incorporated composites (3%, 6%, 9%, 12%, and 15% GO by weight) reveal notable modifications in vibrational behavior following GO integration. As shown in Figure 16, pristine MOF-199 displays sharp and well-defined bands in the 500–1700 cm^{-1} region, corresponding mainly to C=C and C–O stretching modes of the organic linker, together with characteristic metal-ligand vibrations at lower wavenumbers. Upon the introduction of GO NShs, the overall spectral intensity increases and several peaks exhibit

measurable broadening, indicative of enhanced phonon scattering and changes to electron-phonon coupling within the hybrid network [6,10]. The characteristic D and G bands of GO gradually emerge and begin to overlap with intrinsic MOF-199 vibrational modes, becoming especially prominent at GO loadings above ~12%. This increasing prominence reflects the growing contribution of GO's graphitic and defect-related vibrations within the composite. Moreover, the spectral evolution suggests stronger interfacial interactions—such as π–π stacking, electronic coupling, and local structural perturbations—between GO and the MOF framework. These interactions introduce additional vibrational disorder while simultaneously reinforcing the hybrid interface, consistent with reported behavior in MOF-carbon composite systems [35].

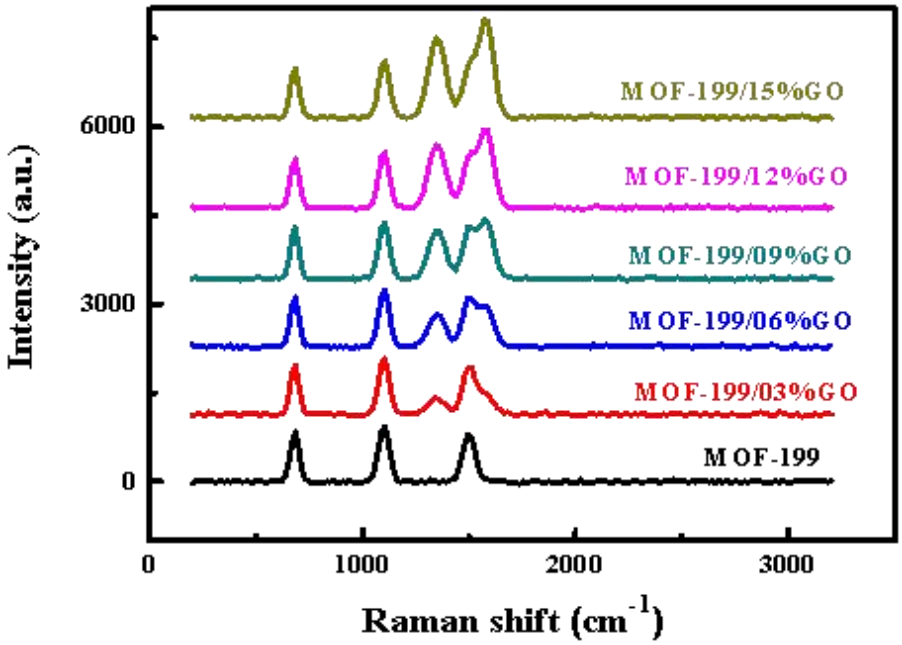

Figure 16. Raman spectra of pristine MOF-199 and MOF-199/GO NCs with varying GO content.

The progressive increase in baseline intensity with higher GO content indicates improved light absorption and scattering, likely resulting from synergistic interactions between the conductive GO network and the porous crystalline framework of MOF-199. Despite these changes, the fundamental vibrational features of MOF-199 remain fully preserved across all compositions, confirming that incorporation of GO does not disrupt the intrinsic structural integrity of the framework. Instead, GO serves to modulate the local vibrational environment without altering the core lattice. These findings provide mechanistic insight into how 2D carbon-based nanofillers interact with 3D MOF architectures and highlight the potential for tailoring optoelectronic and photocatalytic properties through controlled GO incorporation [35,36].

3.9. Textural and porosity characteristics of MOF-199/GO NCs

The textural properties of pristine MOF-199 and the MOF-199/GO NCs were systematically evaluated through nitrogen adsorption-desorption isotherms, BET specific surface area, and total pore volume analyses. The isotherm profiles reveal that all samples retain the intrinsic microporous nature of MOF-199, while the incorporation of GO introduces additional mesoporosity, as evidenced by enhanced nitrogen uptake and mild hysteresis at higher relative pressures. Both the BET surface area and total pore volume increase with GO loading up to an optimal content of 6 wt%, indicating improved pore accessibility and the formation of interfacial voids between MOF crystallites and GO sheets [23]. Beyond this optimal loading, a gradual decline in these textural parameters is observed, likely due to pore blockage, GO restacking, or agglomeration effects that hinder nitrogen diffusion. Overall, these results demonstrate that controlled GO incorporation is an

effective strategy to tune the porosity and surface characteristics of MOF-199, with moderate GO contents yielding the most favorable textural properties [37,38].

3.9.1. Nitrogen adsorption-desorption behavior of MOF-199 and MOF 199/GO NC

Figure 17 presents the nitrogen adsorption-desorption isotherms of pristine MOF-199 and the MOF-199/06% GO composite measured at 77 K. Both materials exhibit a rapid nitrogen uptake at low relative pressures (p/p_0 < 0.1), characteristic of a predominantly microporous structure associated with the intrinsic framework of MOF-199. In comparison to the pristine sample, the MOF-199/06% GO composite demonstrates a higher adsorption capacity throughout the entire pressure range, indicating enhanced surface accessibility and pore volume resulting from the incorporation of GO. At intermediate and high relative pressures, a gradual increase in adsorption accompanied by a modest hysteresis loop is observed, suggesting the presence of additional mesoporous features likely arising from interfacial voids between MOF particles and GO NShs. These results confirm that the introduction of an optimal amount of GO effectively improves the textural properties of MOF-199 while preserving its fundamental microporous nature.

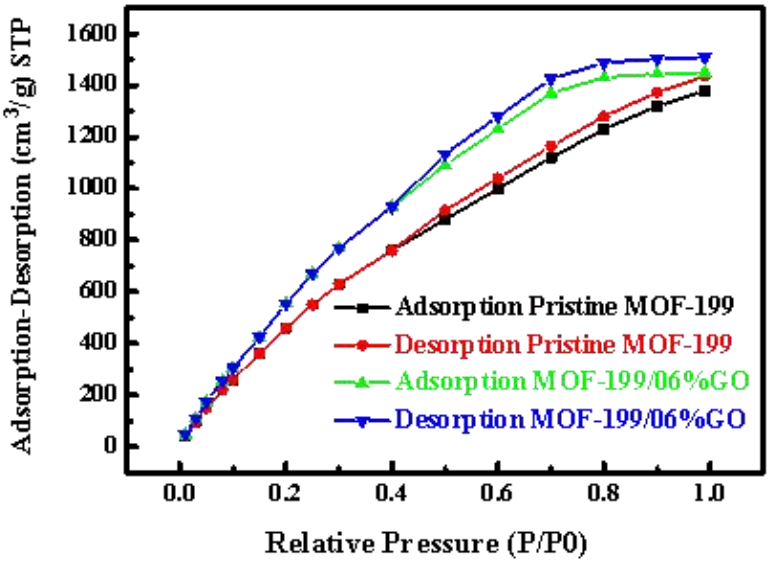

Figure 17. N_2 adsorption-desorption isotherms of pristine MOF-199 and MOF-199/06% GO at 77 K.

3.9.2. Effect of GO loading on the BET surface area of MOF-199

Figure 18 illustrates the dependence of the BET specific surface area of pristine MOF-199 and MOF-199/GO NCs on GO loading. The pristine MOF-199 exhibits a high surface area, which increases progressively upon the introduction of GO, reaching a maximum at 6 wt% GO. This enhancement is attributed to improved dispersion of MOF crystallites and the generation of additional accessible surface sites and interfacial porosity induced by the GO NShs. However, further increases in GO content beyond this optimal loading result in a gradual decline in surface area, likely due to partial pore blockage, aggregation of GO layers, or reduced accessibility of the intrinsic microporous framework. These findings indicate that an appropriate GO content is critical for optimizing the surface area of MOF-199-based composites [13,17].

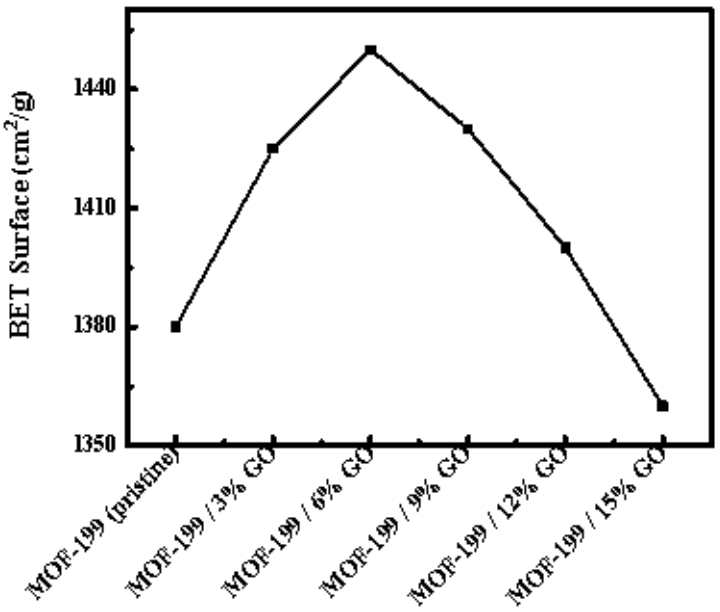

Figure 18. Variation of BET specific surface area of MOF-199 and MOF-199/GO NCs with GO content.

3.9.3. Influence of GO incorporation on the pore volume of MOF-199

Figure 19 presents the variation in total pore volume of pristine MOF-199 and MOF-199/GO NCs with increasing GO content. The pristine MOF-199 displays a considerable pore volume, which increases progressively upon the addition of GO and reaches a maximum at 6 wt% GO [19]. This behavior suggests that moderate GO incorporation promotes the development of additional accessible pores and interfacial voids, leading to a more open and interconnected pore network. However, further increases in GO loading beyond the optimal level result in a noticeable reduction in total pore volume, likely due to partial pore obstruction, restacking of GO NShs, or aggregation effects that limit nitrogen accessibility. These results highlight the critical role of GO content in tailoring the porosity of MOF-199-based composites and are consistent with the trends observed in BET surface area analysis.

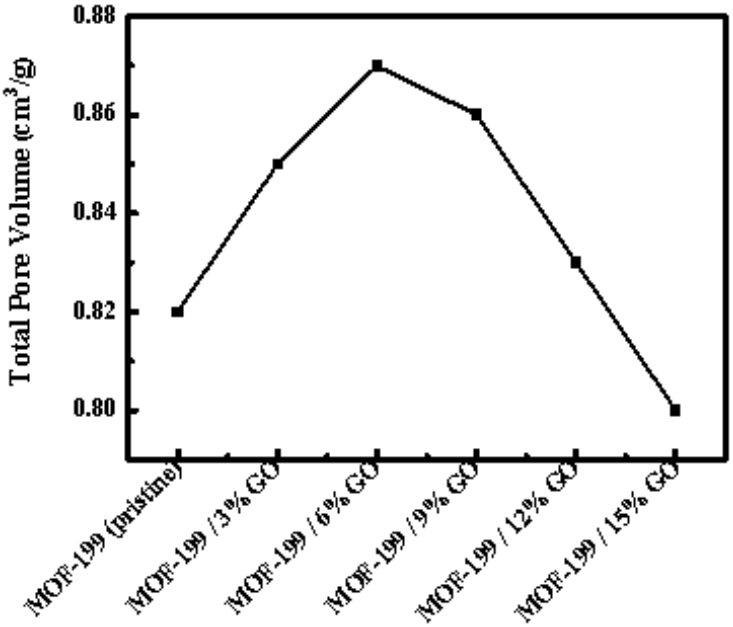

Figure 19. Total pore volume of pristine MOF-199 and MOF-199/GO NCs as a function of GO content.

3.10. Adsorption isotherms and kinetics behavior of MOF-199/GO NCs

The adsorption behavior of pristine MOF-199 and its GO-enhanced NCs was investigated using equilibrium isotherm and kinetic analyses at an initial MB concentration of 10 mg L^{-1}. The isotherm results demonstrate that the incorporation of GO significantly enhances the adsorption capacity, with composites containing 9%–12% GO exhibiting the highest uptake. This improvement is attributed to the synergistic effects of increased porosity, enlarged specific surface area, and the introduction of additional active sites arising from strong interfacial interactions between MOF-199 and GO [36,37]. In contrast, a further increase in GO content to 15% results in a slight reduction in adsorption performance, which can be ascribed to partial pore blockage and nanosheet aggregation that limit accessible adsorption sites. Kinetic modeling using the pseudo-first-order (PFO), pseudo-second-order (PSO), and intraparticle diffusion (IPD) models reveals that the PSO model provides the best fit for all samples, indicating that chemisorption is the dominant adsorption mechanism. For both pristine MOF-199 and the GO-containing composites, adsorption proceeds rapidly during the initial stage due to abundant available active sites, followed by a slower phase where IPD becomes the rate-limiting step. Throughout the entire series, the MOF-199/GO NCs exhibit consistently higher adsorption rates and capacities compared to pristine MOF-199. These results highlight the critical role of GO in modulating adsorption pathways and confirm the strong potential of MOF-199/GO NCs for high-efficiency water purification applications [38–40].

3.10.1. Isotherm behavior of MOF-199/GO NCs

Figure 20 presents the adsorption isotherms for pristine MOF-199 and its GO-modified composites. For all materials, the equilibrium adsorption capacity (qe) increased with the equilibrium concentration (C_e), reflecting effective adsorption behavior. Pristine MOF-199 exhibited the lowest uptake, whereas incorporating GO notably enhanced performance. The composites containing
9%–12% GO achieved the highest adsorption capacities, exceeding 150 mg g^{-1}. This improvement is attributed to the increased porosity, expanded surface area, and the additional active sites generated through the cooperative interactions between MOF-199 and GO NShs. A slight decline in capacity was observed for the 15% GO sample, likely caused by nanosheet aggregation or partial blockage of accessible pores. Overall, these findings demonstrate that the introduction of an optimal amount of GO substantially reinforces the adsorption efficiency of MOF-199, positioning the resulting composites as strong candidates for advanced adsorption-based applications [36,39].

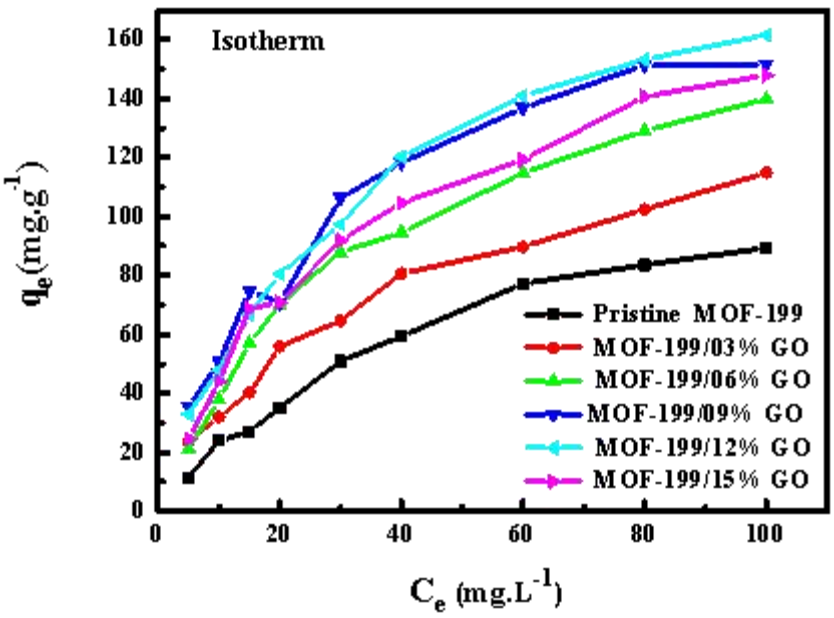

Figure 20. Adsorption isotherms of pristine MOF-199 and MOF-199/GO NCs at different GO loadings.

3.10.2. Enhanced adsorption kinetics of MOF-199/GO NCs compared to pristine MOF-199

Figure 21(a) and Figure 21(b) illustrate the adsorption kinetics of MB on pristine MOF-199 and MOF-199/15% GO NC, respectively, together with fittings to the PFO, PSO, and IPD models. In both systems, a rapid initial uptake is observed within the first few minutes, followed by a slower approach to equilibrium, reflecting the progressive saturation of available adsorption sites. For pristine MOF-199 (Figure 21(a)), the PSO model provides a significantly better fit to the experimental data than the PFO model across the entire adsorption period, particularly during the initial fast adsorption stage [32,34]. This behavior suggests that the adsorption process is predominantly governed by chemisorption involving surface functional groups and coordinatively unsaturated metal sites. The IPD curve does not pass through the origin, indicating that intraparticle diffusion contributes to the overall mass-transfer process but is not the sole rate-limiting step. In the case of the MOF-199/15% GO NC (Figure 21(b)), a higher adsorption capacity and faster kinetic response are clearly observed compared to pristine MOF-199.

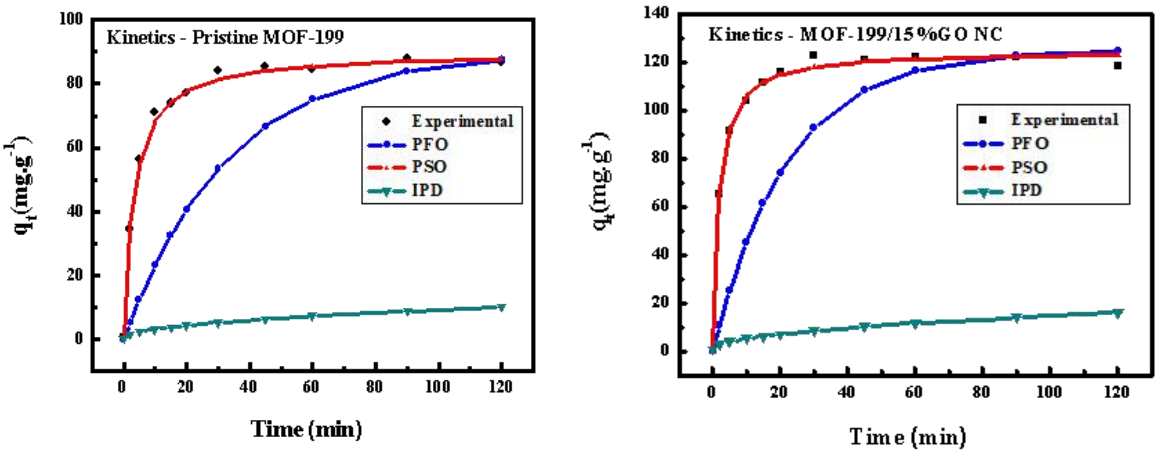

(a) (b)

Figure 21. (a) Kinetic modeling of MB adsorption on pristine MOF-199; (b) kinetic modeling of MB adsorption on MOF-199/15% GO NC.

The PSO model again shows the closest agreement with the experimental data, confirming that the dominant adsorption mechanism remains unchanged after GO incorporation. However, the enhanced kinetic performance reflects the increased density of oxygen-containing functional groups and improved interfacial interactions introduced by GO, which facilitate stronger adsorbate-adsorbent interactions. Similar to pristine MOF-199, the IPD behavior suggests a multi-step adsorption process involving both surface adsorption and diffusion effects. Overall, the comparative kinetic analysis demonstrates that GO incorporation significantly enhances adsorption efficiency and rate while preserving the chemisorption-dominated mechanism, in agreement with the structural and surface chemistry characterization [31,36].

3.10.3. Tuning GO content to modulate the kinetic adsorption performance of MOF-199-based hybrids

Figure 22 presents the experimental adsorption kinetics of MB on pristine MOF-199 and MOF-199/GO NCs containing 3, 6, 9, 12, and 15 wt.% GO. All samples exhibit a rapid initial adsorption stage within the first 10–20 min, followed by a slower approach to equilibrium, indicating progressive saturation of accessible adsorption sites. Pristine MOF-199 shows the lowest

equilibrium adsorption capacity, whereas incorporation of GO markedly enhances both adsorption rate and capacity.

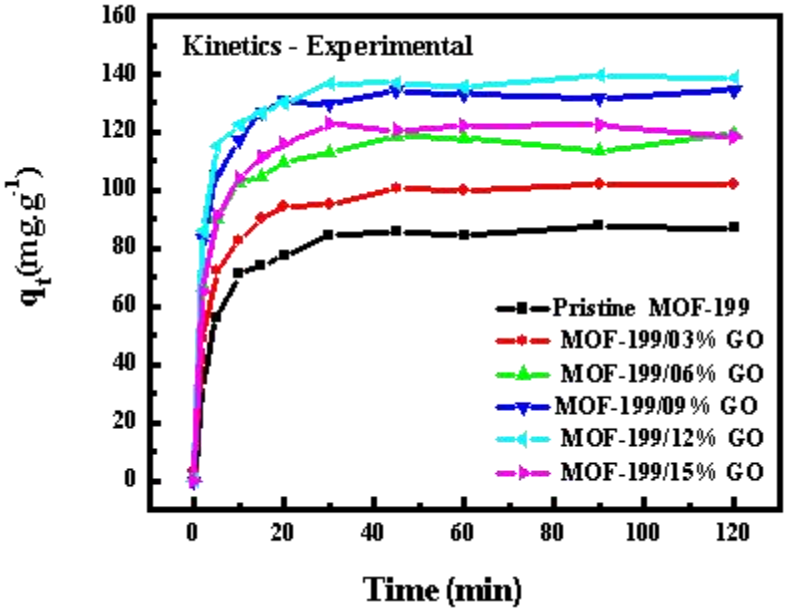

Figure 22. Comparative experimental adsorption kinetics of MB on pristine MOF-199 and MOF-199/GO NCs with varying GO loadings.

The adsorption performance increases with GO loading up to 9–12 wt.%, reaching a maximum equilibrium uptake of approximately 135–140 mg g^{-1}. This improvement is attributed to the synergistic contribution of MOF-199 porosity and GO-derived oxygen-containing functional groups, which promote electrostatic attraction, π–π interactions, and improved mass transfer. At higher GO content (15 wt.%), a slight reduction in adsorption capacity is observed, suggesting partial pore blocking or restacking of GO sheets that limits effective access to MOF pores [35,36,40]. The unified presentation in Figure 22 enables direct comparison across all compositions and clearly demonstrates the existence of an optimal GO loading range. These trends are consistent with the kinetic model analysis and textural characterization, confirming that controlled GO incorporation enhances adsorption efficiency without compromising the intrinsic adsorption mechanism [33,40].

3.10.4. PFO kinetic analysis of MOF-199/GO NCs

Figure 23 presents the PFO kinetic profiles for MB adsorption onto pristine MOF-199 and MOF-199/GO NCs containing 3, 6, 9, 12, and 15 wt% GO. All samples exhibit a rapid initial adsorption stage followed by a slower approach to equilibrium, reflecting the progressive occupation of available surface sites. Compared with pristine MOF-199, the GO-containing composites show markedly enhanced adsorption rates and higher equilibrium uptake, indicating the beneficial role of GO incorporation. Among the composites, the MOF-199/12% GO sample demonstrates the highest adsorption capacity and the fastest kinetic response under the PFO model, suggesting an optimal balance between accessible surface area, pore availability, and interfacial interactions. Lower GO contents (3%–6%) provide moderate improvement, while excessive GO loading (15%) leads to a slight decline in adsorption performance, likely due to partial pore blockage or agglomeration effects.

The close agreement between experimental data and PFO fitting curves confirms that the adsorption process is governed primarily by concentration-dependent surface interactions during the initial adsorption stage. This comparative kinetic analysis highlights the strong dependence of adsorption efficiency on GO loading and supports the role of GO in accelerating mass transfer and enhancing adsorption kinetics without altering the fundamental adsorption mechanism [34].

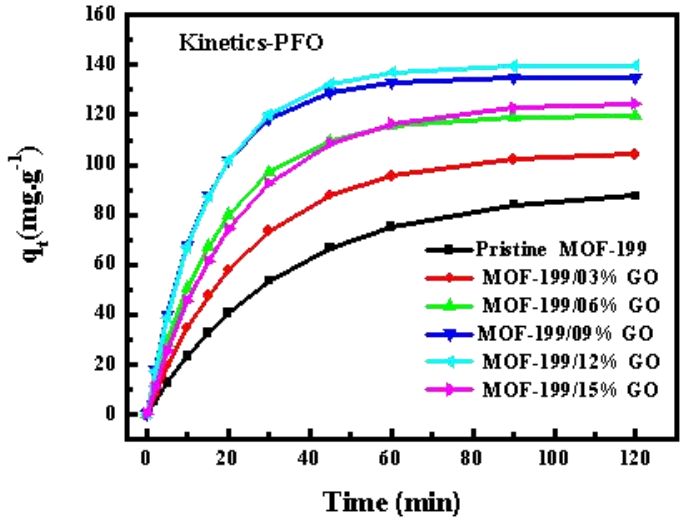

Figure 23. Kinetic profiles of MOF-199 and MOF-199/GO NCs based on the PFO model.

3.10.5. PSO kinetic analysis of MOF-199/GO NCs

Figure 24 illustrates the PSO kinetic fitting for MB adsorption onto pristine MOF-199 and MOF-199/GO NCs with GO loadings of 3, 6, 9, 12, and 15 wt%. All adsorption systems exhibit a rapid initial uptake followed by a gradual approach to equilibrium, indicating fast surface interaction between MB molecules and the available active sites. Compared with pristine MOF-199, all GO-modified samples display higher adsorption capacities and faster attainment of equilibrium, confirming the positive contribution of GO incorporation [37]. The MOF-199/12% GO composite shows the highest equilibrium adsorption capacity and the closest overlap between experimental data and PSO fitting curves, suggesting that this composition provides the most favorable balance between accessible functional groups and pore availability. At lower GO contents (3%–6%), adsorption enhancement is moderate, while excessive GO loading (15%) slightly reduces performance, likely due to partial pore blocking or reduced effective surface exposure. The excellent agreement between the experimental data and the PSO model across all samples indicates that the adsorption process is dominated by chemisorption involving valence forces, such as electron sharing or exchange between MB molecules and oxygen-containing functional groups on GO as well as open metal sites of MOF-199. This result supports the mechanistic interpretation that GO incorporation enhances adsorption primarily by increasing active binding sites rather than merely improving physical diffusion.

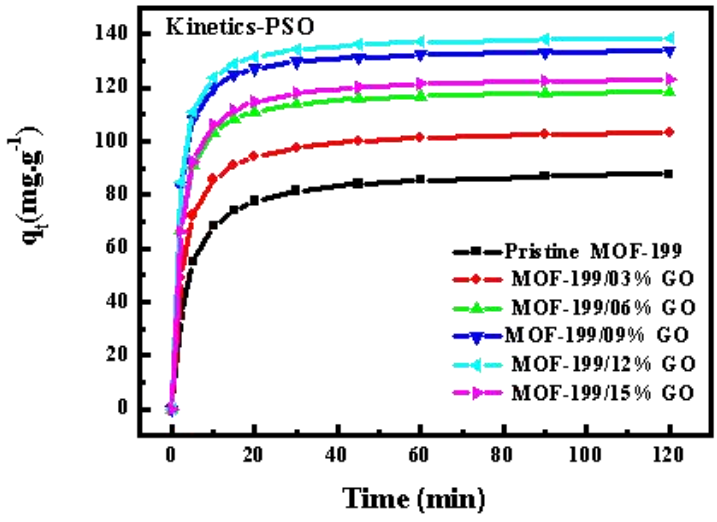

Figure 24. Kinetic profiles of MOF-199 and MOF-199/GO NCs based on the PSO model.

3.10.6. IPD kinetics of pristine and GO-modified MOF-199 NCs

Figure 25 presents the IPD plots for MB adsorption on pristine MOF-199 and MOF-199/GO NCs with varying GO loadings. All samples exhibit multilinear behavior rather than a single linear fit passing through the origin, indicating that IPD is involved in the adsorption process but does not solely control the overall rate. The initial steeper region corresponds to rapid external surface adsorption and boundary-layer diffusion, followed by a second, more gradual linear segment associated with diffusion of MB molecules into the internal pores of the adsorbents. Notably, the IPD lines for GO-containing composites display higher slopes than pristine MOF-199, reflecting enhanced mass-transfer kinetics arising from the increased surface functionality and improved pore accessibility imparted by GO incorporation [38]. However, the clear deviation from the origin (non-zero intercepts) confirms that film diffusion and surface chemical interactions play a significant role alongside IPD. When considered together with the superior fitting of the PSO model, these results provide strong mechanistic evidence that MB adsorption on MOF-199/GO NCs is governed by a mixed diffusion-chemisorption process rather than purely physical diffusion.

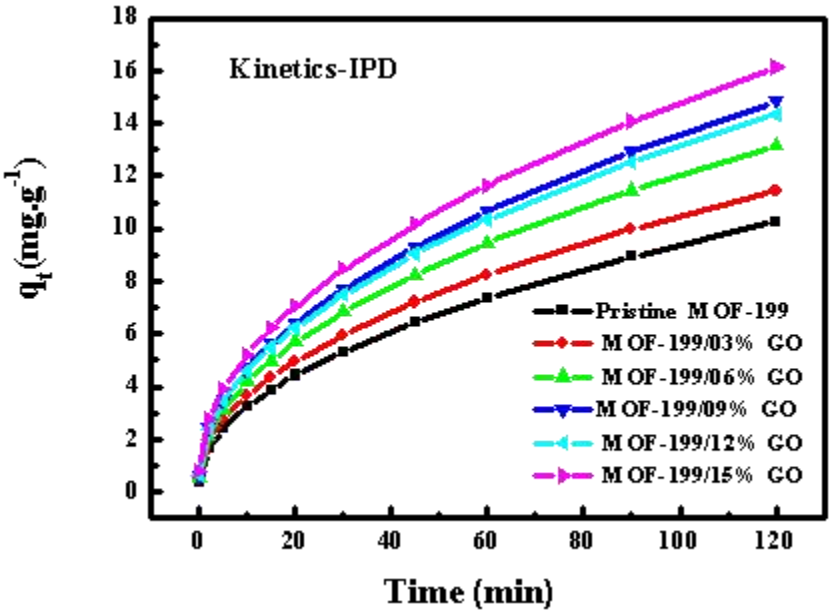

Figure 25. IPD kinetic profiles of pristine MOF-199 and GO-incorporated NCs.

4. Conclusions

In this work, pristine MOF-199 nanoparticles and a series of MOF-199/GO NCs were successfully synthesized through environmentally benign routes and systematically investigated to elucidate the influence of GO incorporation on structural, textural, and adsorption properties. Comprehensive characterization confirmed the preservation of the crystalline MOF-199 framework alongside the effective integration of GO NShs, resulting in strong interfacial interactions and improved morphological uniformity. Textural and porosity analyses revealed that pristine MOF-199 exhibits a predominantly microporous structure with a high BET surface area of approximately 1380 $m^2 g^{-1}$ and a total pore volume of 0.82 $cm^3 g^{-1}$. Controlled GO loading led to a pronounced enhancement in porosity, with the optimized MOF-199/GO NCs achieving a maximum BET surface area of ~1450 $m^2 g^{-1}$ and a pore volume of ~0.87 $cm^3 g^{-1}$. This improvement is attributed to increased pore accessibility and the formation of interfacial mesopores between MOF crystallites and GO NShs. However, excessive GO incorporation resulted in a gradual decline in textural parameters due to partial pore blockage and GO restacking, highlighting the importance of optimized composition. Adsorption studies using MB as a model contaminant demonstrated a direct correlation between enhanced textural properties and adsorption performance, with the

MOF-199/GO NCs exhibiting an adsorption capacity increase of approximately 20%–25% relative to pristine MOF-199 at optimal GO contents (9–12 wt.%). Kinetic and isotherm analyses indicated that the adsorption process is governed by chemisorption, as evidenced by PSO, favorable Langmuir fitting, and spectroscopic signatures confirming strong interactions between dye molecules, open Cu^{2+} metal sites, and oxygen-containing functional groups on GO. Overall, this study establishes a clear structure-textural-performance relationship for MOF-199/GO NCs and demonstrates that controlled GO incorporation is an effective strategy for enhancing adsorption efficiency while maintaining structural stability. The environmentally friendly synthesis approach, combined with the superior adsorption performance of the optimized nanocomposite, highlights the strong potential of MOF-199/GO materials as sustainable and scalable adsorbents for advanced water purification applications.

Declarations

Acknowledgments: The authors acknowledge the Physics Department, Faculty of Science, Suez University, P.O. Box 43221, Suez, Egypt, for providing the facilities and technical support necessary to carry out this research. The authors also gratefully acknowledge E. R. Shaaban for valuable scientific discussions and support.

Availability of Data and Materials: The data used and analyzed during the current study are available from the corresponding author upon reasonable request.

Funding: This research received no external funding.

Author Contributions: **A.M.** conceived and designed the study, conducted the principal experimental work, performed data analysis and interpretation, and prepared the original manuscript. **M.A.I.** and **H.A.Y.** contributed to the experimental work, data analysis, and discussion of the results. **A.A.** contributed to the interpretation of the results and revision of the manuscript. All authors contributed to editorial changes in the manuscript, reviewed the manuscript, and approved the final version of the manuscript. All authors have read and agreed to the published version of the manuscript.

Conflicts of Interest: The author declare no conflict of interest.

References

1. Nguyen, L.T.L.; Nguyen, T.T.; Nguyen, K.D.; et al. Metal-organic framework MOF-199 as an efficient heterogeneous catalyst for the aza-Michael reaction. *Applied Catalysis A: General* 2012, 425–426, 44–52. https://doi.org/10.1016/j.apcata.2012.02.045
2. Kardani, F.; Mirzajani, R.; Ramezani, Z. Determination of nanomolar dissolved polycyclic aromatic hydrocarbons in different water and wastewater samples using a metal-organic framework-199@ graphene oxide fiber and headspace solid-phase microextraction. *Desalination and Water Treatment* 2019, 144, 99–115. https://doi.org/10.5004/dwt.2019.23489
3. Zhang, H.Y.; Shi, R.H.; Zhang, Z.R.; et al. Modification of a Copper-Based Metal-Organic Framework with Graphene Oxide for the Removal of Sulfur Compounds. *European Journal of Inorganic Chemistry* 2018, 2018(24), 2768–2775. https://doi.org/10.1002/ejic.201800133
4. Zheng, Y.; Zheng, S.S.; Xue, H.G.; et al. Metal-organic frameworks/graphene-based materials: Preparations and applications. *Advanced Functional Materials* 2018, 28(47), 1804950. https://doi.org/10.1002/adfm.201804950
5. Issa, R.; Ibrahim, F.A.; Al-Ghoul, M.; et al. Controlled growth and composition of multivariate metal-organic frameworks-199 via a reaction-diffusion process. *Nano Research* 2021, 14(2), 423–431. http://hdl.handle.net/10938/25480
6. Li, J.; Lv, Q.; Bi, L.; et al. Metal-organic frameworks as superior adsorbents for pesticide removal from water: The cutting-edge in characterization, tailoring, and application potentials. *Coordination Chemistry Reviews* 2023, 493, 215303. https://doi.org/10.1016/j.ccr.2023.215303
7. Furukawa, H.; Cordova, K.E.; O'Keeffe, M.; et al. The chemistry and applications of metal–organic frameworks. *Science* 2013, *341*(6149), 1230444. https://doi.org/10.1126/science.1230444

8. Hou, X.D.; Wang, L.C.; Guo, Y. Recent developments in solid-phase microextraction coatings for environmental and biological analysis. *Chemistry Letters* 2017, 46(10), 1444–1455. https://doi.org/10.1246/cl.170366
9. Liu, Y.J.; Wang, Z.; Sun, M. Advances in Composites for Solid-Phase (Micro) Extraction. In: Ikhmayies SJ (editor). Advanced Composites. Springer Nature Switzerland; 2023. pp. 59–92.
10. Rahmati, Z.; Khajavian, R.; Mirzaei, M. Anisotropy in metal–organic framework thin films. *Inorganic Chemistry Frontiers* 2021, 8(14), 3581-3586. https://doi.org/10.1039/D1QI00300C
11. Georgiadis, A.G.; Charisiou, N.; Yentekakis, I.V.; et al. Hydrogen sulfide (H_2S) removal via MOFs. *Materials* 2020, 13(16), 3640. https://doi.org/10.3390/ma13163640
12. Calvin, I.J.; Makuba, G.; Kiende, M.; et al. Metal-Organic Frameworks as a New Frontier in Biogas Production and Purification: Recent Trends. Heliyon 2024; Under Review.
13. Mostafa, M.Y.A.; Mostafa, A.; Abdel-Rahman, M.; et al. XRD peak broadening modelling for Al-alloys characterization compared with Rietveld profile analysis. Materials Today: Proceedings 2023; In Press.
14. Iqbal, M.Z.; Shaheen, M.; Khan, M.W.; et al. Exploring MOF-199 composites as redox-active materials for hybrid battery-supercapacitor devices. *RSC advances* 2023, 13(5), 2860–2870. https://doi.org/10.1039/D2RA06457J
15. Roshdy, M.A.; Ataallah, M.A.; Khedr, A.I.; et al. Spatial interpolation and isotherms studies for groundwater remediation utilizing Be/CNTs@ Alg NC material; case study: Beni-Suef aquifer floodplain. *Environmental Earth Sciences* 2025, 84(13), 365. https://doi.org/10.1007/s12665-025-12342-w
16. Hadi, Y.A.A.; Ghazala, M.S.A.; Yousef, S.A.; et al. Raman spectroscopy of unknown mineral sample by solar pumped laser system. *Journal of Physics: Conference Series* 2020, *1472*, 012006. https://doi.org/10.1088/1742-6596/1472/1/012006
17. Zhang, H.Y.; Zhang, Z.R.; Yang, C.; et al. A Computational Study of the Adsorptive Removal of H_2S by MOF-199. *Journal of Inorganic and Organometallic Polymers and Materials* 2017, 28(3), 694–701. https://doi.org/10.1007/s10904-017-0740-4
18. Liang, Z.; Liang, Y.; Yu, P.; et al. Ultrasonic-assisted in situ synthesis of MOF-199 on the surface of carboxylated cellulose fibers for efficient adsorption of methylene blue. *RSC advances* 2024, 14(21), 15095–15105. https://doi.org/10.1039/d4ra02099e
19. Liu, Z.; Yang, S.L.; Wang, Z.W.; et al. Construction of hydrophobic HKUST-1 in wood with selective adsorption performance for toluene and moisture blends. *Separation and Purification Technology* 2025, 357, 130134. https://doi.org/10.1016/j.seppur.2024.130134
20. Liu, B.; Shioyama, H.; Akita, T.; et al. Metal-organic framework as a template for porous carbon synthesis. *Journal of the American Chemical Society* 2008, *130*(16), 5390–5391. https://doi.org/10.1021/ja7106146
21. Wang, C.; Yin, H.; Tian, P.; et al. Remarkable adsorption performance of MOF-199 derived porous carbons for benzene vapor. *Environmental Research* 2020, 184, 109323. https://doi.org/10.1016/j.envres.2020.109323
22. Attar, O.J.; Alrubaye, R.T.A. Synthesis and characterization of a contemporary type of metal-organic framework and its application for purification wastewater from toxic methylene blue dye. *Journal of Ecological Engineering* 2024, 25(1), 37–48. https://doi.org/10.12911/22998993/173209
23. Mostafa, M.Y.A.; Mostafa, A.; Abdel-Rahman, M.; et al. XRD peak broadening modelling for Al-alloys characterization compared with Rietveld profile analysis. Materials Today: Proceedings 2023; In Press.
24. Chen, M.; Chen, J.; Liu, Y.; et al. Enhanced adsorption of thiophene with the GO-modified bimetallic organic framework Ni-MOF-199. *Colloids and Surfaces A: Physicochemical and Engineering Aspects* 2019, 578, 123553. https://doi.org/10.1016/j.colsurfa.2019.06.019
25. Aguila-Rosas, J.; Cano, F.J.; Nagaya, A.; et al. MOF-Composites for adsorption and degradation of contaminants in wastewater. *Chemical Communications* 2025, 61(63), 11706-11731. https://doi.org/10.1039/D5CC02843D
26. Meng, X.M.; Dai, Z.D.; Jia, C.Q.; et al. Hierarchical porous MOF-199 and zeolite composites with high adsorption performance for both toluene and acetone. *Industrial & Engineering Chemistry Research* 2023, 62(46), 19702–19714. https://doi.org/10.1021/acs.iecr.3c02910
27. Zhao, G.; Huang, X.; Tang, Z.; et al. Polymer-based nanocomposites for heavy metal ions removal from aqueous solution: A review. *Polymer Chemistry* 2018, *9*, 3562–3582. https://doi.org/10.1039/C8PY00484F

28. Martínez Gil, J.M.; Vivas Reyes, R.; Bastidas-Barranco, M.; et al. Biodiesel production from transesterification with lipase from Pseudomonas cepacia immobilized on modified structured metal–organic materials. *ACS Omega* 2022, *7*(46), 41882–41904. https://doi.org/10.1021/acsomega.2c02873
29. Lirio, S.; Liu, W.L.; Lin, C.L.; et al. Aluminum based metal-organic framework-polymer monolith in solid-phase microextraction of penicillins in river water and milk samples. *Journal of Chromatography A* 2016, 1428, 236–245. https://doi.org/10.1016/j.chroma.2015.05.043
30. Shen, M.; Forghani, F.; Kong, X.; et al. Antibacterial applications of metal-organic frameworks and their composites. *Comprehensive Reviews in Food Science and Food Safety* 2020, 19(4), 1397–1419. https://doi.org/10.1111/1541-4337.12515
31. Abbaszadeh, A.; Tadjarodi, A. Speciation analysis of inorganic arsenic in food and water samples by electrothermal atomic absorption spectrometry after magnetic solid phase extraction by a novel MOF-199/modified magnetite nanoparticle composite. *RSC Advances* 2016, 6(114), 113727–113736. https://doi.org/10.1039/C6RA21819A
32. Zhang, W.; Huang, T.; Ren, Y.; et al. Preparation of chitosan crosslinked with metal-organic framework (MOF-199)@ aminated graphene oxide aerogel for the adsorption of formaldehyde gas and methyl orange. *International Journal of Biological Macromolecules* 2021, 193, 2243–2251. https://doi.org/10.1016/j.ijbiomac.2021.11.056
33. Li, Y. Research progress of hydrogen sulfide adsorption based on MOFs. *ChemistrySelect* 2021, 6(37), 9960–9968. https://doi.org/10.1002/slct.202102950
34. Zhang, S.J.; Liu, L.; Yang, J.Y.; et al. Pd-Ru-Bi nanoalloys modified three-dimensional reduced graphene oxide/MOF-199 composites as a highly efficient electrocatalyst for ethylene glycol electrooxidation. *Applied Surface Science* 2019, 492, 617–625. https://doi.org/10.1016/j.apsusc.2019.06.228
35. Guo, Y.P.; Xie, W.; Li, H.; et al. Construction of hydrophobic channels on Cu (I)-MOF surface to improve selective adsorption desulfurization performance in presence of water. *Separation and Purification Technology* 2022, 285, 120287. https://doi.org/10.1016/j.seppur.2021.120287
36. Shah, A.H.; Yuan, C.; Hao, W.Y.; et al. Adsorption kinetics of simulated mixture wastewaters over porous Bi2MoO6@ BiOCl@ MOF-199 heterostructure. *Journal of Solid State Chemistry* 2022, 307, 122835. https://doi.org/10.1016/j.jssc.2021.122835
37. Mansour, E.A.; Taha, M.; Mahmoud, R.K.; et al. A combined experimental and computational studies on thiophene adsorption from liquid fuels over ZIF-67@ ZnFe LDH composites. *Materials Chemistry and Physics* 2025, 334, 130499. https://doi.org/10.1016/j.matchemphys.2025.130499
38. Deng, Y.X.; Vellingiri, K.; Kim, K.H.; et al. Activation strategies of metal-organic frameworks for the sorption of reduced sulfur compounds. *Chemical Engineering Journal* 2018, 350, 747–756. https://doi.org/10.1016/j.cej.2018.06.006
39. Li, M.; Li, Y.W.; Li, W.; et al. Synthesis and application of Cu-BTC@ ZSM-5 composites as effective adsorbents for removal of toluene gas under moist ambience: Kinetics, thermodynamics, and mechanism studies. *Environmental Science and Pollution Research* 2020, 27(6), 6052–6065. https://doi.org/10.1007/s11356-019-07293-2
40. Ma, X.L.; Wang, W.L.; Sun, C.G.; et al. Adsorption performance and kinetic study of hierarchical porous Fe-based MOFs for toluene removal. *Science of The Total Environment* 2021, 793, 148622. https://doi.org/10.1016/j.scitotenv.2021.148622